GEORG-AUGUST-UNIVERSITÄT
GÖTTINGEN

Fakultät für
Physik

Master's Thesis

Studien zur Messung der Topquark-Masse mit der Matrixelement-Methode im semileptonischen Kanal

Studies for a top quark mass measurement using the matrix element method in the semileptonic channel

prepared by

Carsten Brachem

from Sögel

at the II. Physikalisches Institut

Thesis number:	II.Physik-UniGö-MSc-2012/01
Thesis period:	29th August 2011 until 28th February 2012
First referee:	Prof. Dr. Arnulf Quadt
Second referee:	Prof. Dr. Ariane Frey

Contents

1. Introduction **1**

2. Theoretical background **3**
2.1. The Standard Model . . . 3
2.2. Top quark physics . . . 5
2.2.1. Hadron collider physics . . . 5
2.2.2. Top pair production . . . 6
2.2.3. Single top production . . . 7
2.2.4. Decay channels . . . 8
2.2.5. Measurable properties . . . 10

3. Experimental setup **15**
3.1. The Large Hadron Collider . . . 15
3.2. The ATLAS Detector . . . 16
3.2.1. Prerequisites and Coordinate system . . . 17
3.2.2. The Magnets . . . 18
3.2.3. The Inner Detector . . . 19
3.2.4. The Calorimeter system . . . 20
3.2.5. The Muon detector . . . 22
3.2.6. The Trigger and Data Acquisition systems . . . 23
3.2.7. Current status . . . 24

4. The Matrix Element Method **25**
4.1. The differential cross section as a production likelihood . . . 25
4.2. Accommodating finite detector resolution . . . 26
4.2.1. Transfer functions . . . 26
4.2.2. Detector acceptance . . . 27
4.3. The event likelihood . . . 27
4.4. Parameter estimation . . . 28
4.5. Application of the matrix element method in this analysis . . . 28

5. The transfer functions **31**
5.1. Gaussian transfer functions . . . 31
5.2. Mc10b transfer functions . . . 34
5.2.1. Transfer function for light jets . . . 34
5.2.2. Transfer function for b-jets . . . 38
5.2.3. Transfer function for electrons . . . 38
5.2.4. Transfer function for muons . . . 40

6. MEMTool **43**
6.1. Details of the integration process . . . 43
6.1.1. Numerical integration with VEGAS . . . 44
6.1.2. Integration variables and phase space transformations . . . 45
6.2. MEMTool's components . . . 46
6.2.1. Matrix elements . . . 46
6.2.2. Transfer functions . . . 47
6.2.3. Parton distribution functions . . . 48
6.2.4. Integration variables . . . 48
6.3. Default configuration . . . 51

7. Tests with simulated parton level events **53**
7.1. Results with unsmeared data . . . 54
7.2. Results with Gaussian transfer functions . . . 57
7.3. Results with Mc10b transfer functions . . . 61

8. Tests with ATLAS Monte Carlo events **65**

9. Systematic uncertainties **71**

10. Conclusion and outlook **73**

A. Phase space transformations and reconstruction of event kinematics **75**
A.1. SimplePznuKinematic . . . 75
A.2. WmassKinematic . . . 77
A.3. FourMassesKinematic . . . 77

1. Introduction

The matrix element method is a measurement technique which has been developed by the DØ collaboration for a precise measurement of the top quark mass [1]. It has been used at the Tevatron with great success, for example in the most precise single top quark mass measurement from DØ with a relative uncertainty of under 0.9% [2].
This thesis describes the method in general and especially its application for a top quark mass measurement in the semileptonic channel in the ATLAS experiment at the LHC.

After a brief overview of the standard model of particle physics with an emphasis on top quark physics in Chapter 2, the experimental setup is presented: the Large Hadron Collider and the ATLAS detector, one of its experiments, with its various subsystems, are described in Chapter 3. Chapter 4 describes the matrix element method in general, and afterwards its application for this thesis. Transfer functions – distributions that model the detector response for different objects and energies – are components that are needed for the matrix element method. They are described in Chapter 5. Chapter 6 introduces MEMTool, a computer programme that has been developed to perform the measurement of the top quark mass with the matrix element method. Tests of the method have been performed on simulated parton-level events for various configurations and on official ATLAS Monte Carlo events. The results of these tests are presented in Chapters 7 and 8. Chapter 9 gives a brief overview over systematic uncertainties. Chapter 10 finally sums up the results.

2. Theoretical background

2.1. The Standard Model

The Standard Model of particle physics is a collection of theories that accurately describe the strong, weak and electromagnetic interactions between all known subatomic particles.

The theories contained in the Standard Model, all local gauge-invariant quantum field theories, are quantum electrodynamics, the Glashow-Weinberg-Salam theory of electroweak processes and quantum chromodynamics. Quantum electrodynamics is a gauge theory with the symmetry group U(1) which describes electromagnetic interactions. The Glashow-Weinberg-Salam theory of electroweak processes is a unified description of electromagnetism and the weak interaction, which is described by the groups $\mathrm{SU}(2)_L \times \mathrm{U}(1)_Y$. Quantum chromodynamics (QCD), described by the $\mathrm{SU}(3)_C$ gauge group, is the theory which describes the strong interaction. The last of the four known fundamental forces, gravity, is not considered in the Standard Model [3].

Generation	Flavour		Charge [e]	Mass [MeV/c^2]	Lifetime [s]
first	$\begin{pmatrix}\nu_e\\ e\end{pmatrix}$	(e neutrino)	0	≈ 0	∞
		(electron)	-1	0.51	∞
second	$\begin{pmatrix}\nu_\mu\\ \mu\end{pmatrix}$	(μ neutrino)	0	≈ 0	∞
		(muon)	-1	105.66	$2.20 \cdot 10^{-6}$
third	$\begin{pmatrix}\nu_\tau\\ \tau\end{pmatrix}$	(τ neutrino)	0	≈ 0	∞
		(tau)	-1	1776.99	$2.91 \cdot 10^{-13}$

Table 2.1.: Table of all leptons. If not stated otherwise, masses are always given in MeV/c^2. Likewise, electrical charges are always given in units of the proton charge [3].

The Standard Model describes the interactions between the twelve known spin-$\frac{1}{2}$ fermions, which are grouped into six quarks and six leptons, which are then in turn grouped

Generation	Flavour		Charge [e]	Mass [MeV/c^2]
first	$\begin{pmatrix} u \\ d \end{pmatrix}$	(up)	$2/3$	3
		(down)	$-1/3$	7
second	$\begin{pmatrix} c \\ s \end{pmatrix}$	(charm)	$2/3$	1200
		(strange)	$-1/3$	120
third	$\begin{pmatrix} t \\ b \end{pmatrix}$	(top)	$2/3$	173000
		(bottom)	$-1/3$	4300

Table 2.2.: Table of all quarks (Listed quark masses are imprecise and are just given as an overview. Especially the light quark masses are speculative.) [3].

into three generations. The first generation of leptons contains the well-known electron and the electron neutrino. The leptons of the second generation are the muon and its corresponding neutrino, those of the third generation are the tau and the tau neutrino. All leptons are listed in Table 2.1.
The first generation of quarks are the up and down quark, which make up the commonly known protons and neutrons; the second and third generation contain the more exotic charm and strange quark, and the top and bottom quark, respectively. All quarks are listed in Table 2.2.

Force	Mediator	Charge [e]	Mass [MeV/c^2]	Lifetime [s]
Strong	g (8 gluons)	0	0	∞
Electromagnetic	γ (photon)	0	0	∞
Weak	$W^{\pm}$ (charged)	± 1	$80,420$	$3.11 \cdot 10^{-25}$
	Z^0 (neutral)	0	$91,190$	$2.64 \cdot 10^{-25}$

Table 2.3.: Table of all gauge bosons [3].

Forces are mediated by gauge bosons. The force carriers of the strong force are the eight gluons, which act only on quarks and other gluons (or, to be more precise, on particles with a colour charge). Electromagnetism is mediated by the photon and acts on all particles with an electric charge. The $W^{\pm}$ bosons and the Z^0 boson are the mediators of the electroweak force. A list of all gauge bosons is shown in Table 2.3.

Initially, all particles in the Standard Model are described as massless particles. Masses for neither the fermions and the massive gauge bosons $W^{\pm}$ and Z^0 cannot be introduced

ad-hoc, because it would violate local gauge invariance.
One way to give them mass is the so-called Higgs mechanism, in which the bosons acquire mass through spontaneous symmetry breaking [4].
A scalar field with a non-zero vacuum expectation value is introduced. By spontaneously breaking the symmetry of this Higgs field, mass terms are introduced to the Lagrangian without violating gauge invariance.

The fermions are given mass by a Yukawa interaction between the Higgs field and the fermion Dirac fields.
The excitation of the Higgs field is called Higgs boson. This particle has not been observed yet, but is being searched for at the LHC and the Tevatron in order to either confirm or reject the Higgs mechanism.

2.2. Top quark physics

With a mass of 173.2 ± 0.9 GeV/c^2, the top quark is by far the heaviest of the quarks, weighing over 40 times more than the bottom quark, the second heaviest quark [5].
It was discovered in 1995 by the CDF and DØ experiments at the Tevatron accelerator at the Fermi National Accelerator Laboratory near Chicago [6, 7]. Due to its mass, the top quark has some special properties. It has a very short lifetime of the order of 10^{-25} s, which is too short for it to form bound states, such as a bound $t\bar{t}$ or $t\bar{b}$ state. Thus, one has direct access to spin information of a produced $t\bar{t}$ pair, for example to measure the W boson's helicity. Through loop corrections, the masses of the W boson, the top quark and the Higgs boson are connected. Therefore, with a precise measurement of the top quark mass m_t and by using the precise measurement of the W boson mass m_W from LEP, one can set constraints on the possible Higgs mass.
In the following, the production mechanisms for top quark pairs as well as single top quarks at hadron colliders are explained, followed by a description of the top quark's decay channels. Afterwards, an overview of measurements of top quark properties is given.

2.2.1. Hadron collider physics

The LHC is a proton-proton collider. The interacting protons consist of valence quarks, sea quarks and gluons, each carrying only a fraction of the proton's momentum. The distribution of these fractions is modeled by so-called parton distribution functions or PDFs. Figure 2.1 shows a plot of the CTEQ6 leading order PDF, which is used in this analysis, for various parton flavours [8].

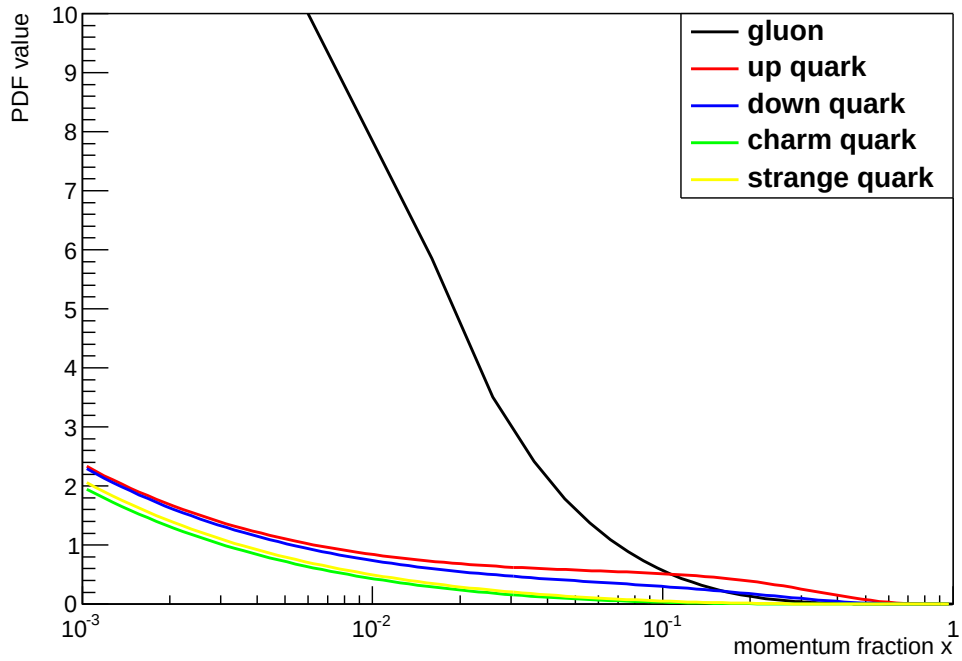

Figure 2.1.: Plot of the CTEQ6 PDF for gluons and up, down, charm and strange quarks at $Q = 3500$ GeV [8].

In order to obtain the hadronic differential cross section of a given hard scattering process, one must convolute its differential cross section $\mathrm{d}\sigma_{hs}$ with the PDFs and summed over all possible initial state particles i and j:

$$\mathrm{d}\sigma = \sum_{i,j \in \text{flavours}} \int_0^1 \int_0^1 f_i(x_1) f_j(x_2) \mathrm{d}\sigma_{hs}(x_1, x_2) \mathrm{d}x_1 \mathrm{d}x_2 \quad , \tag{2.1}$$

where x_1 and x_2 are the initial particles' fractions of the protons' momenta and $f_i(x)$ is the probability density of a particle i to have a momentum fraction of x.

2.2.2. Top pair production

At hadron colliders, top-antitop ($t\bar{t}$) pairs can be produced via the strong interaction. The two possible processes at leading order are quark-antiquark annihilation (see Figure 2.2(a)) and gluon-gluon fusion (see Figure 2.2(b)).

While at the Tevatron $t\bar{t}$ pairs were mostly produced by the first process, the latter one dominates at the LHC. The theoretically predicted cross sections for both processes and accelerators are listed in Table 2.4.

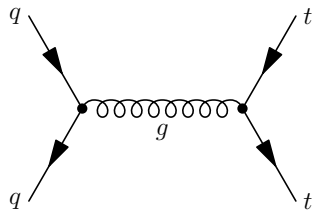

(a) $t\bar{t}$ production via $q\bar{q}$ annihilation.

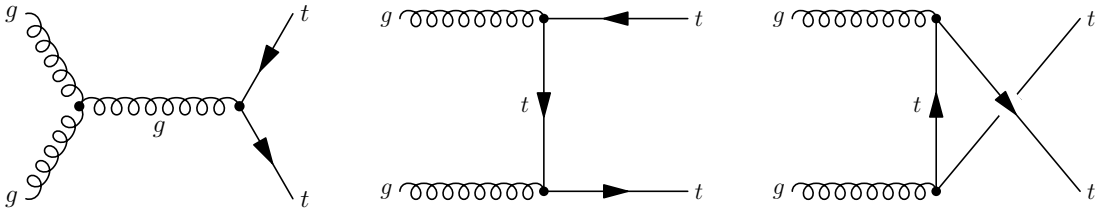

(b) $t\bar{t}$ production via gg fusion.

Figure 2.2.: Leading order Feynman diagrams for the strong production of $t\bar{t}$ pairs via $q\bar{q}$ annihilation and gg fusion.

Accelerator	$\sqrt{s}$ [TeV]	$\sigma_{t\bar{t}}$ [pb]
Tevatron	1.96	$7.08^{+0.36}_{-0.42}$
LHC	7	163^{+10}_{-13}
	10	415^{+31}_{-19}
	14	918^{+64}_{-41}

Table 2.4.: Theoretical cross sections of $t\bar{t}$ pair production at the Tevatron and the LHC for their respective centre-of-mass energies. The calculations were done at approximated NNLO level using the MSTW2008 NNLO pdf with an assumed top mass of $m_t = 173$ GeV [9–11].

2.2.3. Single top production

Single top quarks can be produced via weak interactions in the processes shown in Figure 2.3. The single top quark production was discovered in 2009 by the CDF and DØ collaborations at the Tevatron [12, 18]. Of the three production processes, the t-channel production (see Figure 2.3(a)) is the most common one with an expected cross section of 1.14 pb at the Tevatron and an expected cross section of 149 pb at the LHC at $\sqrt{s} = 14$ TeV. This is the only channel that has been observed up to this date. The two other channels, associated production of a top quark and a W boson (see Figure 2.3(b)) and s-channel production (see Figure 2.3(c)), are also expected to have a larger cross section at the LHC than at the Tevatron.

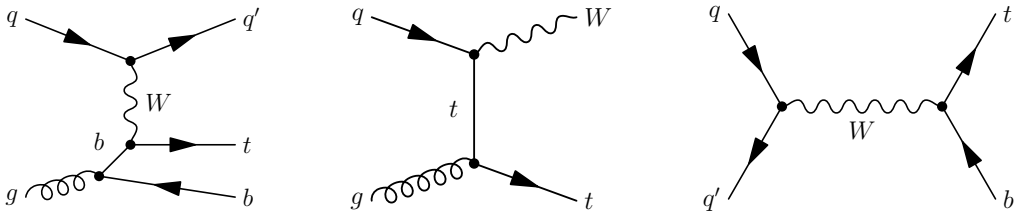

(a) t-channel (b) associated Wt production (c) s-channel

Figure 2.3.: Leading order Feynman diagrams for the weak production of single top quarks [12, 13].

Accelerator	$\sqrt{s}$ [TeV]	$\sigma_{t\text{-channel}}$ [pb]	σ_{Wt} [pb]	$\sigma_{s\text{-channel}}$ [pb]
Tevatron	1.96	1.14 ± 0.06	0.14 ± 0.03	0.53 ± 0.02
LHC	7	$41.9^{+0.9}_{-0.6}$	$7.8 \pm 0.2^{+0.5}_{-0.6}$	$3.17 \pm 0.06^{+0.13}_{-0.10}$
	10	130^{+5}_{-5}	$19.4 \pm 0.5^{+1.0}_{-1.1}$	$5.16 \pm 0.09^{+0.20}_{-0.14}$
	14	149 ± 6	43 ± 5	$7.7^{+0.6}_{-0.5}$

Table 2.5.: Theoretical cross sections of single top production for the t-channel, associated Wt production and the s-channel at the Tevatron and the LHC for their respective centre-of-mass energies. The cross sections for antitop quarks differ for the s-channel at the LHC [10, 14–17].

The predicted cross sections for single top quark production are listed in Table 2.5.

The weak production of top quarks is dependent on the absolute value of the CKM matrix element $|V_{tb}|$ and is thus a viable source for measurements of this quantity.

2.2.4. Decay channels

The top quark decays almost instantaneously with a branching ratio of about 100% into a W boson and a bottom quark. In the following, a branching ratio of 100% is assumed for this decay.
The b quark then hadronizes and forms a jet, while the W boson can decay either leptonically, that is into a charged lepton and its corresponding (anti-)neutrino, or hadronically, which means a decay into a quark-antiquark pair.
This yields three possible decay channels for a $t\bar{t}$ pair.

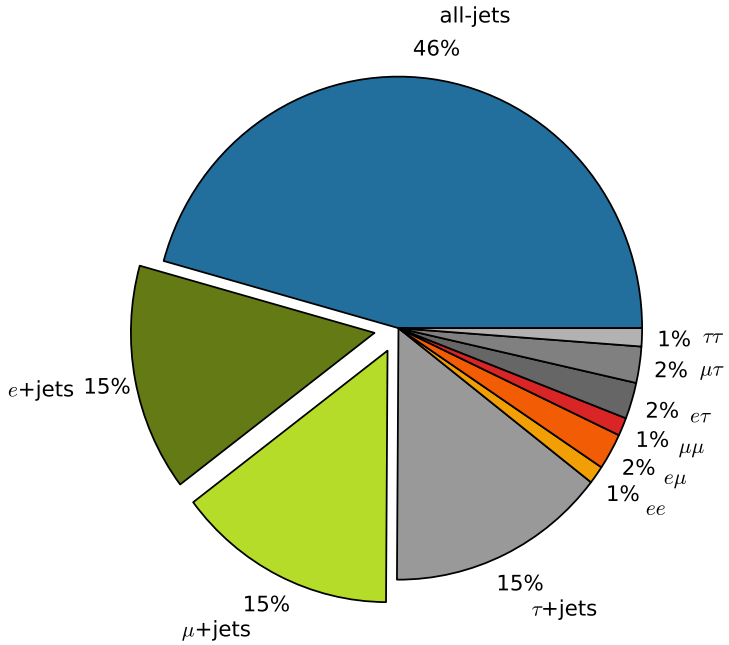

Figure 2.4.: Decay channels with approximate branching ratios for the $t\bar{t}$ decay. [19]

The dileptonic channel

In the **dileptonic** channel, both W bosons decay leptonically. Its signature is two leptons, two b-jets and missing energy. This channel has a low background, but it is also the one with the lowest branching ratio and has two neutrinos (from the two leptonic W decays) which are difficult to be reconstructed from missing energy.

The semileptonic channel

In the **semileptonic** channel, also called the **lepton+jets** channel, one W boson decays hadronically and the other one decays leptonically. Also referred to as the "golden channel", it has a reasonable branching ratio and moderate background. Its signature is a lepton, four jets (with two of them being b-jets) and missing energy from a neutrino.

The all-jets channel

In the **all-jets** channel, both W bosons decay hadronically. This channel has a signature of four light quark jets and two b-jets. It has the highest branching ratio of all three channels, but also the highest background.

A chart of the branching ratios of the $t\bar{t}$ decay channels is shown in Figure 2.4.
The branching ratios for the channels, according to [19], are:

$$\begin{aligned} \mathrm{BR}(\mathrm{all-jets}) &= 45.7\% \\ \mathrm{BR}(\ell + \mathrm{jets}) &= 29.2\% \\ \mathrm{BR}(\mathrm{dilepton}) &= 4.7\% \end{aligned}$$

Decays containing a tau lepton are left out of these branching ratios, as taus are not detected directly.

2.2.5. Measurable properties

Mass

The top quark is by far the heaviest of all quarks and even the heaviest of all elementary particles. The most precise value for its mass up to date is $m_t = 173.2 \pm 0.9$ GeV/c^2, combining several single measurements of the CDF and DØ collaborations [5]. A plot of the single measurements and their combination is shown in Figure 2.5.
With a relative precision of below 0.6% it is thus the most precisely measured quark mass.

A precise measurement, together with a precise measurement of the W boson mass, allows to make predictions on the mass of the Higgs boson [20].

According to electroweak theory, the W boson mass can be calculated at tree level to

$$M^2_{W,\mathrm{tree}} = \frac{\hbar^3}{c} \cdot \frac{\pi\alpha}{\sqrt{2}G_F} \cdot \left(1 - \left(\frac{M_W^2}{M_Z^2}\right)\right)^{-1} \quad . \tag{2.2}$$

In order to account for radiative loop corrections, the W boson mass from equation (2.2) has to be divided by a factor of $(1 - \Delta r)$:

$$M^2_W = \frac{\hbar^3}{c} \cdot \frac{\pi\alpha}{\sqrt{2}G_F} \cdot \frac{1}{\left(1 - \left(\frac{M_W^2}{M_Z^2}\right)\right)(1 - \Delta r)} \quad . \tag{2.3}$$

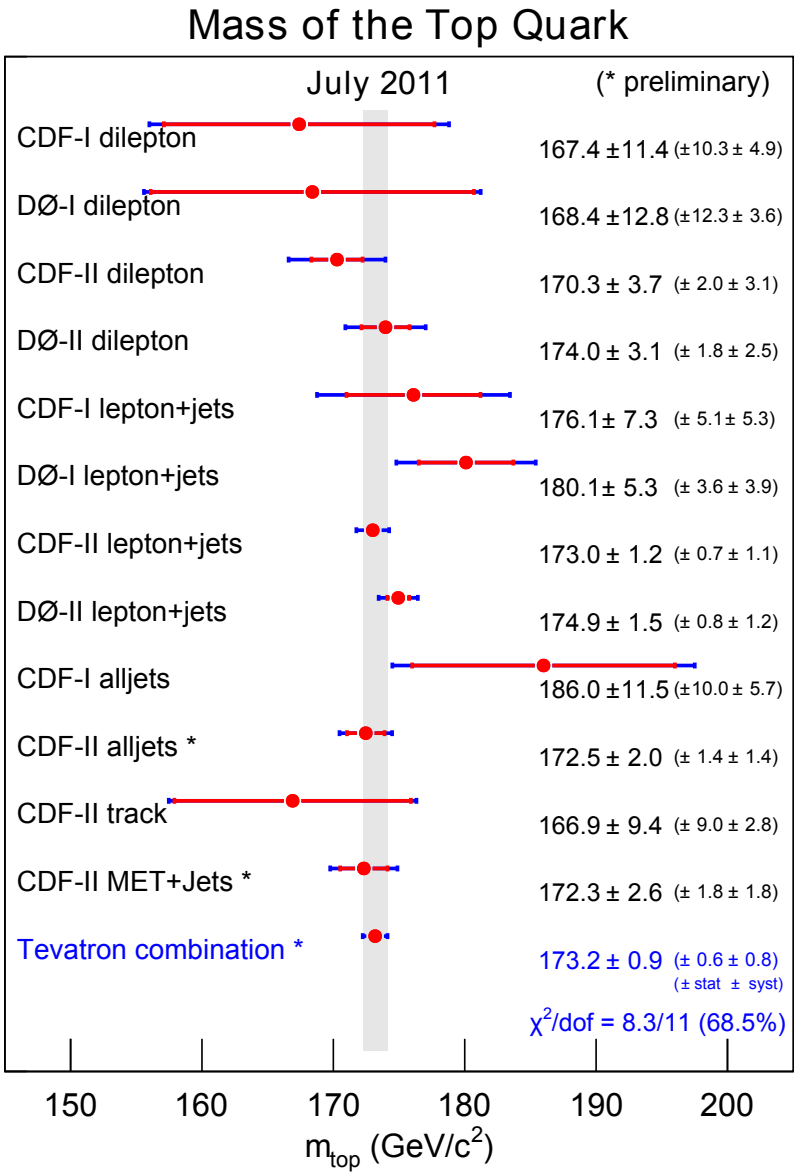

Figure 2.5.: The most recent combination of single top mass measurements from the CDF and DØ collaborations [5].

The loop corrections in Δr have contributions that include the top quark mass as well as the Higgs boson mass,

$$(\Delta r)_{\text{top}} \sim m_t^2 \qquad \text{and} \qquad (\Delta r)_{\text{Higgs}} \sim \ln\left(\frac{m_H^2}{M_Z^2}\right) \quad ,$$

making the Higgs mass dependent on the top and the W boson mass. This dependence is illustrated in Figure 2.6 together with results of measurements of M_W and m_t.

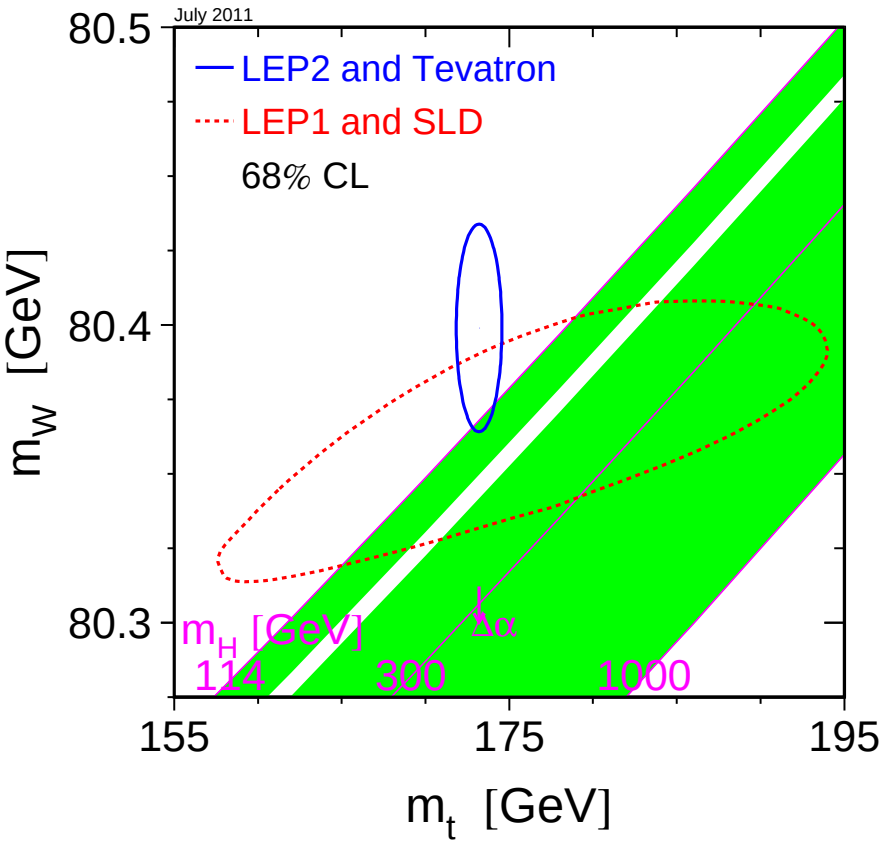

Figure 2.6.: Plot of the Higgs mass' dependence on m_t and M_W. 68% confidence level limits from LEP and Tevatron results are also shown [21].

Cross section

The top cross section measurement is yet another test for Standard Model predictions. Additionally, a too large cross section for $t\bar{t}$ or single t production could be a hint for new physics processes, such as the existence of a charged Higgs, a W' boson or flavour-

changing neutral currents. The cross sections of single top processes are directly related to the top quark's Cabbibo-Kobayashi-Maskawa (CKM) matrix element V_{tb}, i.e. they are proportional to $|V_{tb}|^2$.
Precise cross section measurements from the Tevatron [22] and results from the LHC [23–29] are in good agreement with Standard Model predictions.
Even without assuming unitarity or constraining the number of quarks, $|V_{tb}|$ is measured to be [30]

$$|V_{tb}| = 0.88 \pm 0.07 \qquad ;$$

the 95% CL lower limit on $|V_{tb}|$ is 0.77.

W helicity

The well-defined spin state of the $t\bar{t}$ system allows a measurement of the helicity of the W boson. In the Standard Model, a W boson originating from a top decay must have either zero or negative helicity due to the $V-A$ structure of the weak interaction. The fraction of the W bosons with zero helicity can be approximated to

$$f_0 = \frac{\frac{m_t^2}{2m_W^2}}{1 + \frac{m_t^2}{2m_W^2}} \approx 70\% \qquad .$$

Measurements from the Tevatron are in good accordance with this prediction. The combined results from DØ and CDF [31] are

$$\begin{aligned} f_0 &= 0.732 \pm 0.081 \\ f_+ &= -0.039 \pm 0.045 \qquad . \end{aligned}$$

Charge

It has been speculated that the observed top quark was not the predicted Standard Model top quark with an electric charge of $+\frac{2}{3}e$, but rather an exotic one with a charge of $-\frac{4}{3}e$. This possibility has been excluded with a 95% confidence level by now [32].

3. Experimental setup

The following chapter introduces the Large Hadron Collider and the ATLAS detector. The detector's layout and its components will be described as well as the trigger system and the data acquisition systems.

3.1. The Large Hadron Collider

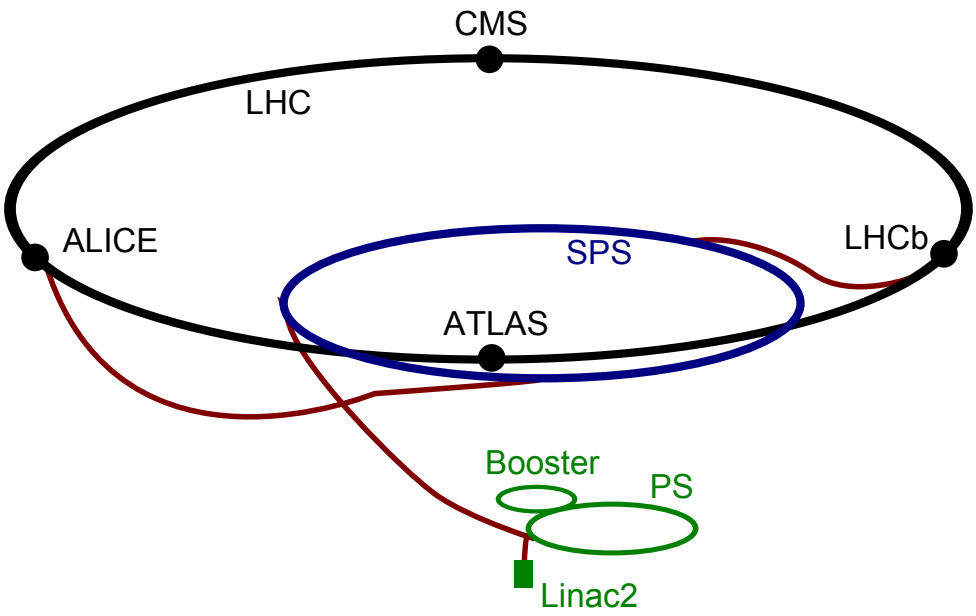

Figure 3.1.: Layout of the LHC experiments and pre-accelerators.

The Large Hadron Collider – or short LHC – is a proton-proton[1] collider at the site of CERN near Geneve in Switzerland. It lies 100 m below the ground and has a circumference of 27 km.
Its design centre-of-mass energy of $\sqrt{s} = 14$ TeV is over seven times higher compared to that of the Tevatron. Although it currently only runs at half of that energy, $\sqrt{s} = 7$ TeV,

[1]In addition to the proton-proton runs, the LHC is also used to accelerate and collide Pb (lead) ions. Since these heavy ion collisions are of no interest to the subsequent analysis, they will not be discussed here.

it allows experimental access to an energy region that was not possible before.
The LHC hosts four large experiments: ALICE, ATLAS, CMS and LHCb. ATLAS (A Torodial LHC ApparatuS) and CMS (Compact Muon Solenoid) are multi-purpose experiments, while ALICE (A Large Ion Collider Experiment) attempts to study quark-gluon plasma and LHCb studies the physics of b-quarks.

Different from the proton-antiproton collider Tevatron, the LHC collides protons and protons. One reason for this is that antiprotons are rare and difficult to produce, another one is that at the LHC's energies, the fraction of gluons contributing to production cross sections is very high.

An illustration of the LHC with its pre-accelerators can be seen in Figure 3.1.
The protons, which are produced by ionizing hydrogen gas, are first accelerated by the linear accelerator LINAC2 to an energy of 50 MeV and then fed into the Proton Synchrotron Booster. From there, having an energy of 1.4 GeV, they are injected into the Proton Synchrotron (PS) and accelerated to an energy of 26 GeV before they enter the Super Proton Synchrotron (SPS) to reach an energy of 450 GeV.
At last, they are injected into the LHC, where after about 20 minutes of further acceleration they reach their peak energy of 7 TeV (3.5 TeV in the current phase). The protons are then brought to collisions at the four collision points inside the experiments.

3.2. The ATLAS Detector

The ATLAS detector is the largest of the four experiments at the LHC. It measures 25 m in height and 44 m in length, weighs approximately 7000 t and is forward-backward symmetric with respect to the interaction point. Its main components are the magnet configuration, the inner detector, the calorimeters, the muon detector and the trigger and data acquisition systems, which will be presented after an introduction to the coordinate system used for the detector.
Detailed information about the ATLAS detector can be found in [33]. A cut-away view of the ATLAS detector can be seen in Figure 3.2.

The ATLAS collaboration is made up of more than 3000 people from 38 countries and more than 174 universities and laboratories.

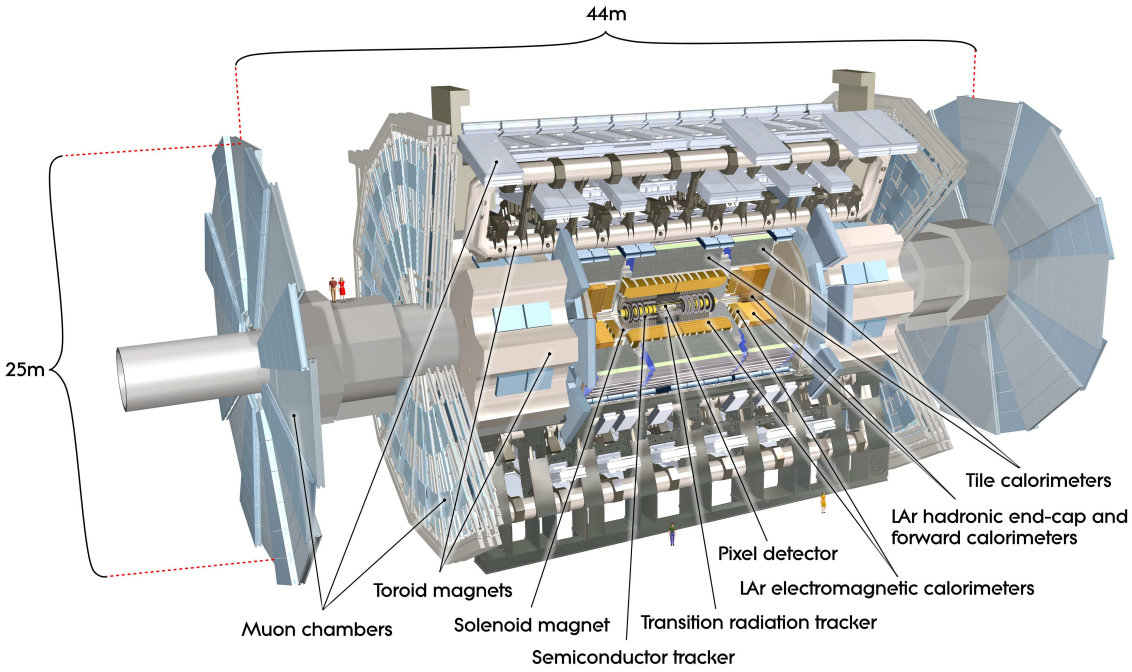

Figure 3.2.: Cut-away view of the ATLAS detector.

3.2.1. Prerequisites and Coordinate system

A right-handed coordinate system is used for coordinate descriptions inside the ATLAS detector. The nominal interaction point constitutes the origin of the coordinate system. The beam direction is defined as the z-axis. Thus, the $x-y$-plane is transverse to the beam direction, with the x-axis being defined as pointing towards the centre of the LHC and the y-axis being defined as pointing upwards. The azimuthal angle ϕ is measured in the $x-y$-plane and the polar angle θ is the angle from the beam axis.
The pseudorapidity η is defined as

$$\eta = -\ln\tan\left(\frac{\theta}{2}\right) \quad .$$

In the case of massive objects, such as jets, the rapidity y, defined as

$$y = \left[2\ln\left(\frac{E+p_z}{E-p_z}\right)\right]^{-1} \quad ,$$

is used. The transverse momentum p_T, the transverse energy E_T and the missing transverse energy E_T^{miss} are defined in the $x-y$-plane.

The definition for p_T is

$$p_T = \sqrt{p_x^2 + p_y^2} \quad ,$$

E_T and E_T^{miss} are defined analogously.
The distance ΔR in the $\eta - \phi$-space is defined as

$$\Delta R = \sqrt{\Delta\eta^2 + \Delta\phi^2} \quad .$$

3.2.2. The Magnets

The magnetic system of the ATLAS detector consists of four superconducting magnets, is 26 m in length and 22 m in diameter and can store an energy of 1.6 GJ. Figure 3.3 shows the layout of the magnets.

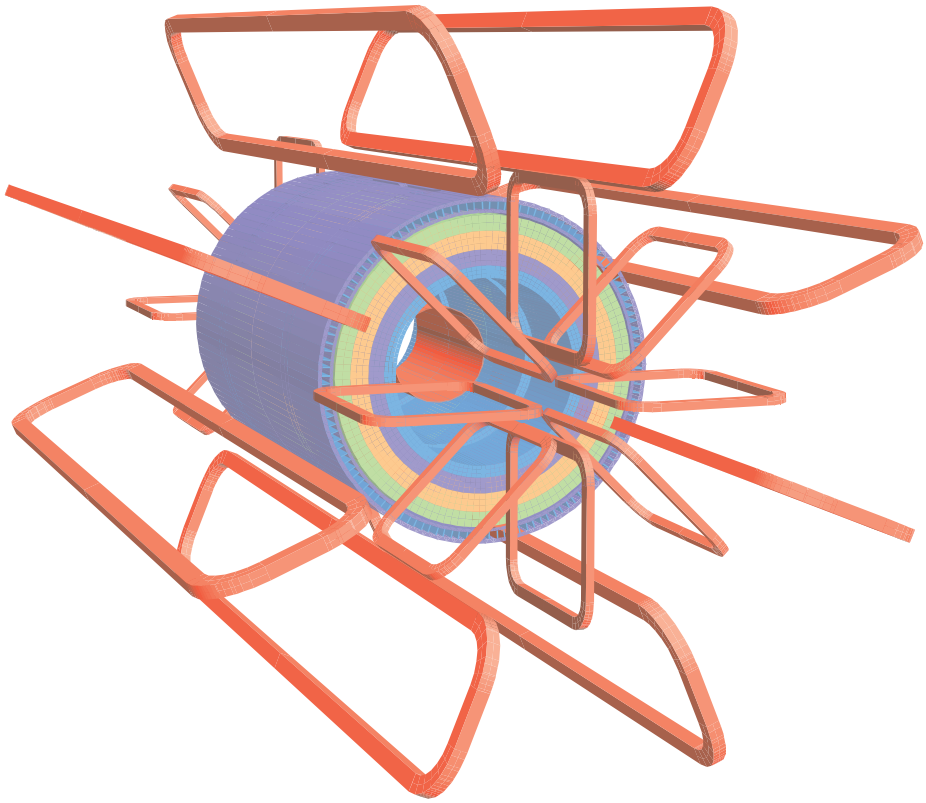

Figure 3.3.: Geometry of magnet windings and tile calorimeter steel. The eight barrel toroid coils, with the end-cap coils interleaved are visible.

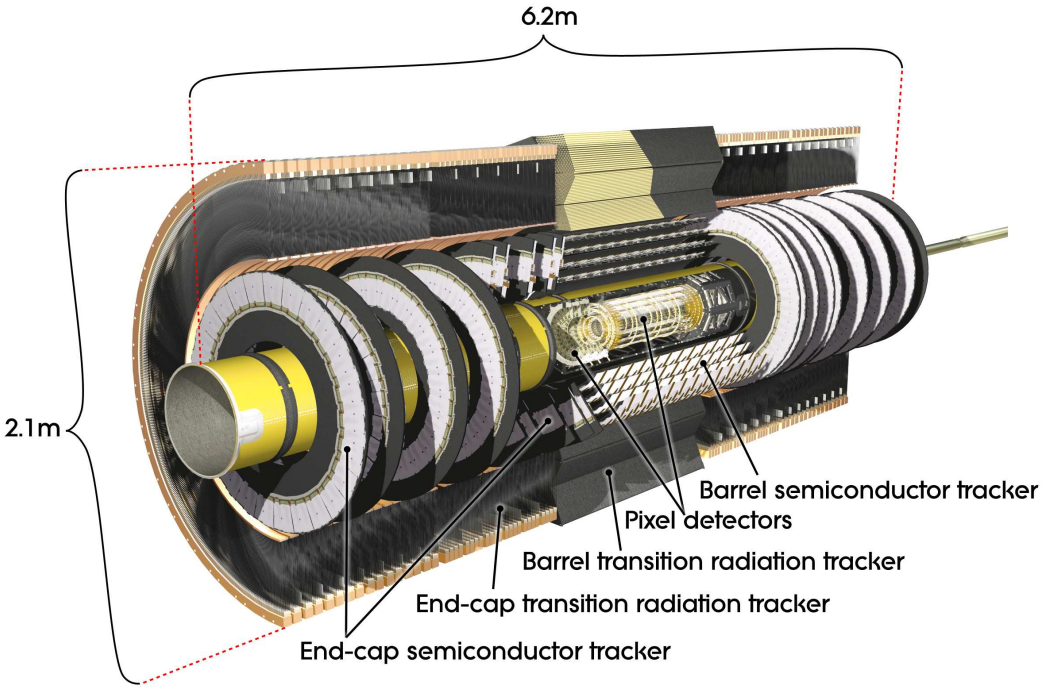

Figure 3.4.: Cut-away view of the ATLAS inner detector.

The two components of the magnetic system are:

- a solenoid magnet at the centre, aligned to the beam axis, which produces a 2 T magnetic field for the inner detector;
- a barrel toroid magnet and two end-cap toroid magnets, arranged with an eightfold azimuthal symmetry around the calorimeters, which provides the muon detectors in the central region with a magnetic field of about 0.5 T and the muon detectors in the end-cap regions with a magnetic field of about 1 T.

3.2.3. The Inner Detector

Particle tracks from the interaction point have to be determined and identified with high precision and accuracy. Also, an identification of the primary vertex and possible secondary vertices is often crucial. This tracking is the purpose of the inner detector's subsystems, the pixel and silicon microstrip (SCT) trackers and the Transition Radiation Tracker (TRT). A cut-away view of the inner detector is shown in Figure 3.4.

The precision tracking detectors – the three-layered pixel detector and the SCT – cover the region $|\eta| < 2.5$. In the barrel region, the detectors are arranged in concentric cylinders aligned to the beam axis, with the pixel detector comprising the innermost layer, followed

by the SCT and the TRT. In the end-cap region, the detectors are located on disks perpendicular to the beam axis.

The Pixel Detector is a highly segmented semiconductor tracker, providing a formidable resolution of 10 μm in $x-\phi$ and 115 μm in z-direction, and was designed to provide good vertex tracking. It consists of $1,744$ sensors with $47,232$ pixels each [33]. The size of one pixel is 50×400 μm^2. The whole pixel detector has approximately 80.4 million readout channels.

The Semiconductor Tracker (SCT) consists of a barrel part containing $2,112$ modules and two end-caps. On its way through the SCT, a track crosses eight strip layers, yielding four space points. In the barrel region, the strips are inclined by a small angle of 40 mrad to allow the measurement of both coordinates, with one set of strips in each layer being aligned parallel to the beam axis. In the end-cap regions, one set of strips is aligned radially and another set with an angle of 40 mrad.
The accuracy per module is 17 μm $(R-\phi)$ and 580 μm (z) for the barrel modules and vice versa for the end-cap modules. The total number of readout channels in the SCT is approximately 6.3 million.

The Transition Radiation Tracker (TRT) consists of drift chamber tubes with a diameter of 4 mm. In the barrel region, the tubes are 144 cm long and aligned parallel to the beam axis. The end-caps have 37 cm long tubes, arranged radially in a wheel pattern. The TRT only provides resolution in $R-\phi$ direction, with an accuracy of 130 μm per tube. Although the spatial resolution of the TRT is lower than those of the pixel detector and the SCT, the TRT can provide an improvement to the tracking because a passing particle will generate up to 36 hits in the tubes. The total number of TRT readout channels is approximately $351,000$.

3.2.4. The Calorimeter system

The calorimeter system of the ATLAS detector covers the region of $|\eta| < 4.9$, using different detectors for different purposes and regions. The electromagnetic calorimeter provides precise energy resolution for electrons and photons, while the hadronic calorimeter provides good energy containment for hadronic showers, though with a coarser granularity. Containment is a crucial aspect for the calorimeters, both for energy resolution and to limit hadrons escaping the hadronic calorimeter into the muon detector on the outside.

[2]This is the minimum size for one pixel and also the actual size for most of them.

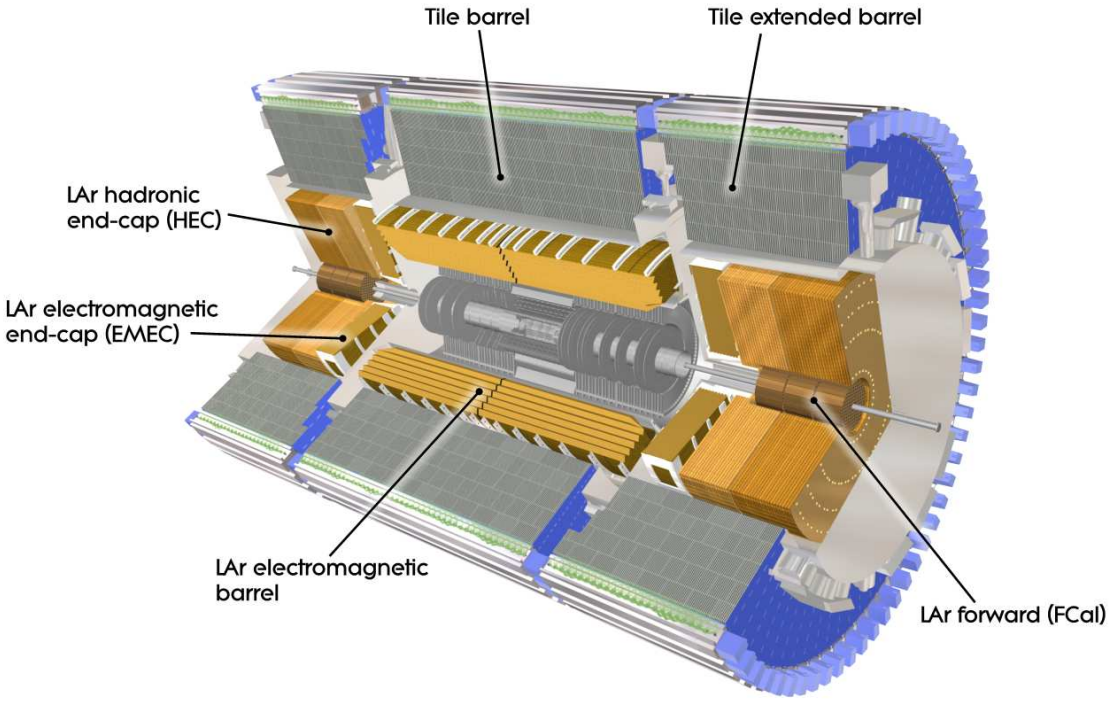

Figure 3.5.: Cut-away view of the ATLAS calorimeter system.

The EM calorimeter provides a thickness of > 22 radiation lengths (X_0) in the barrel and > 24 X_0 in the end-caps.
An overview of the ATLAS calorimeters is shown in Figure 3.5.

The Electromagnetic Calorimeter is, like all calorimeters inside the ATLAS detector, a sampling calorimeter with full ϕ-symmetry and coverage around the beam axis. The EM calorimeter consists of a barrel part ($|\eta| < 1.475$) and two end-caps ($1.375 < |\eta| < 3.2$), both having liquid argon (LAr) as active and lead as passive material. LAr was chosen because of its linear response behaviour, its stability of response over time and its intrinsic radiation-hardness. The electromagnetic calorimeters are cooled by cryostats to a constant temperature of 85 K.
The design energy resolution of the EM calorimeters is

$$\frac{\sigma_E}{E} = \frac{10\%}{\sqrt{E[\text{GeV}]}} \oplus 0.7\% \quad . \tag{3.1}$$

The Hadronic Calorimeter consists of the tile calorimeter in the barrel region, the hadronic LAr end-cap calorimeters and the LAr forward calorimeters.
The tile calorimeter is placed directly outside the EM calorimeter envelope. Its barrel

covers the region $|\eta| < 1.0$ and its two extended barrels the range $0.8 < |\eta| < 1.7$. It is a sampling calorimeter with scintillator tiles as active material and steel as absorber. The scintillator tiles are read out via wavelength shifting fibres into photomultiplier tubes (PMTs). The barrel and the extended barrels are divided azimuthally into 64 modules each.

The Hadronic End-cap Calorimeter (HEC) consists of two independent wheels per end-cap, located directly behind the electromagnetic end-cap calorimeters. They use the same LAr cryostats. Each wheel consists of 32 modules and is divided into two segments in depth, giving a total of four layers per end-cap.

The Forward Calorimeter (FCal) is integrated into the end-cap cryostats. It consists of three modules for each end-cap. The first module is made of copper and optimised for electromagnetic measurements. The other two modules are made of tungsten and mainly measure the energy of hadronic interactions.

The hadronic calorimeters provide a design energy resolution of

$$\frac{\sigma_E}{E} = \frac{50\%}{\sqrt{E[\text{GeV}]}} \oplus 3\% \qquad \text{for the barrel and end-cap, and} \tag{3.2}$$

$$\frac{\sigma_E}{E} = \frac{100\%}{\sqrt{E[\text{GeV}]}} \oplus 10\% \qquad \text{for the forward calorimeter.} \tag{3.3}$$

3.2.5. The Muon detector

The muon spectrometer covers a range of $|\eta| < 2.7$ and provides a trigger on muon events for $|\eta| < 2.4$. In the region with $|\eta| < 1.4$, muon tracks are deflected by the large barrel toroid's magnetic field. For $1.6 < |\eta| < 2.7$, muon tracks are bent by the end-cap magnets. In the transition region of $1.4 < |\eta| < 1.6$, a combination of barrel and end-cap magnets provides the magnetic deflection.

The muon detector comprises four different subsystems: Monitored Drift Tube chambers for tracking and momentum resolution, Cathode Strip Chambers for tracking and Resistive Plate Chambers and Thin Gap Chambers as fast systems for triggering.

The **Monitored Drift Tube** chambers (**MDT**) perform the precision momentum measurement in the $|\eta| < 2.7$ region[3]. Each chamber consists of three to eight drift tubes, which achieve an average resolution of 80 μm. The average resolution per chamber is 35 μm. The maximum drift time for electrons in the MDTs is 700 ns.

The forward region of $2 < |\eta| < 2.7$ uses **Cathode Strip Chambers (CSC)** as the innermost tracking layer due to their higher rate capability and better time resolution of about 7 ns. The 32 CSCs are multi-wire proportional chambers. The resolution of a chamber is 40 μm in R-direction and 5 mm in the transverse plane.

The ability to trigger on muon tracks was an essential design criterion of the muon system. To allow this, fast trigger chambers are part of the muon detector, capable of delivering track information within a few nanoseconds after the passage of a particle. The trigger chambers for the barrel region ($|\eta| < 1.05$) are the 606 **Resistive Plate Chambers (RPC)**, while the end-cap region ($1.05 < |\eta| < 2.4$) is covered by **Thin Gap Chambers (TGS)**. Both RPCs and TGSs have a very low intrinsic response time of 10 ns and 3−7 ns[4], respectively.

3.2.6. The Trigger and Data Acquisition systems

The protons at the LHC interact at an extremely high rate of about 1 GHz, yielding an enormous amount of data, which cannot be stored. To reduce it, a set of criteria is necessary to select "interesting" events and reduce the amount of data to a processable level. The trigger system does exactly this.
It is divided into three different stages: the Level 1 trigger (L1), the Level 2 trigger (L2) and the event filter. Each trigger level refines the decisions made on the previous level and applies additional selection criteria.

The Level 1 trigger uses only information from some of the detector's subsystems, e.g. the muon trigger chambers. It uses this information to accept or reject an event within 2.5 μs, reducing the rate to about 75 kHz. The Level 2 trigger has an event processing time of ≈ 40 ms and reduces the accepted event rate further to approximately 3.5 kHz. The data then goes into the event filter, which reduces the event rate to roughly 200 Hz. Also, the complete event is being built here. The size of an event is around 1.3 MB.

[3] An exception is the innermost end-cap layer where the MDTs' coverage is limited to $|\eta| < 2.0$.
[4] These time resolutions are for the chambers alone without contributions from signal-propagation or electronics.

3.2.7. Current status

The LHC has run with a centre-of-mass energy of $\sqrt{s} = 7$ TeV in 2010 and 2011. In 2010, ATLAS recorded 45.0 pb^{-1} of data. During the 2011 run, ATLAS recorded data with a total integrated luminosity of 5.25 fb^{-1}.
After the current winter shutdown, the LHC will run at an increased centre-of-mass energy of $\sqrt{s} = 8$ TeV in 2012 before it goes into a long shutdown period to prepare for higher energy running. The data target for 2012 is 15 fb^{-1}.

4. The Matrix Element Method

The idea behind the Matrix Element Method is to calculate – for each event – the likelihood that a certain process produces the event's final state observed in the detector.
In the case of this analysis, this is the likelihood that a selected event was produced under the assumption of a certain top quark mass. By doing this for a range of possible top quark masses and combining the likelihoods of many events, one gets a likelihood distribution that uses the final state's full kinematic information to estimate the true top quark mass.

The Matrix Element Method was developed and first used by the DØ collaboration for the measurement of the top quark mass in the lepton+jets channel at Tevatron, yielding the most precise single measurement of the top quark mass to that date [1]. The CDF collaboration has a similar method called the Dynamic Likelihood method [34].

This chapter will describe the Matrix Element Methods and its parts in detail.

4.1. The differential cross section as a production likelihood

The differential cross section for a scattering process with two particles 1 and 2 colliding and producing particles $3, 4, \ldots, n$ with four-momenta p_i is given by Fermi's Golden Rule [3]:

$$\mathrm{d}\sigma_{hs} = \frac{(2\pi)^4 |\mathcal{M}|^2}{4\sqrt{(p_1 \cdot p_2)^2 - m_1^2 m_2^2}} \times \mathrm{d}\Phi_{n-2} \qquad . \tag{4.1}$$

Here, the four-momentum of particle i is denoted by p_i and its (three-)momentum by $\vec{p}_i$. $\mathcal{M}$ is the matrix element of the process. It describes the transition from initial to final state and is a function of all momenta.
$\mathrm{d}\Phi_{n-2}$ is the volume element of the $n-2$ body Lorentz invariant phase space:

$$\mathrm{d}\Phi_{n-2} = \delta^4(p_1 + p_2 - p_3 - \ldots - p_n) \prod_{j=3}^{n} \frac{\mathrm{d}^3\vec{p}_j}{2(2\pi)^3 E_j} \quad . \tag{4.2}$$

The differential cross section in Equation 4.1 is proportional to the probability of this process occuring, but it is only valid for parton interactions. In hadronic interactions, as mentioned in Section 2.2.1, Equation 4.1 has to be convoluted with the PDFs:

$$\mathrm{d}\sigma = \sum_{i_1, i_2 \in \text{flavours}} \int_0^1 \int_0^1 f_{i_1}(x_1) f_{i_2}(x_2) \mathrm{d}\sigma_{hs}(x_1 p_1, x_2 p_2, \ldots) \mathrm{d}x_1 \mathrm{d}x_2 \quad . \tag{4.3}$$

The expression in Equation 4.3 is the differential cross section for one specific final state. To get from this equation to the probability of a certain final state being produced via a certain process, one needs to normalize the differential cross section via the total cross section for the selected process.
The total cross section can be obtained by integrating the differential cross section over the entire phase space:

$$\sigma_{tot} = \int \mathrm{d}\sigma \quad . \tag{4.4}$$

4.2. Accommodating finite detector resolution

4.2.1. Transfer functions

If each and every event could be reconstructed perfectly, the calculation above would be enough. But the ATLAS detector, like every other detector, only has a finite resolution, which has to be accounted for. Also, the events considered in this analysis contain neutrinos, which cannot be detected by ATLAS at all.

To compensate, a transfer function $W(\vec{x}, \vec{y})$ is introduced. $W(\vec{x}, \vec{y})$ is the probability that a final state $\vec{x}$ resulted in a detector response of $\vec{y}$. Usually, the transfer function is a product of single object transfer functions for each object in the final state (e.g. a jet), for example:

$$W(\vec{x}, \vec{y}) = W_{jet}(x_1, y_1) \cdot W_{lep}(x_2, x_2) \ldots$$

Including the transfer function, the differential cross section for an observed state $\vec{y}$ becomes:

$$\mathrm{d}\sigma_{obs}(\vec{y}) = \int_{\vec{x}} \mathrm{d}\sigma(\vec{x}) W(\vec{x}, \vec{y}) \mathrm{d}\vec{x} \qquad . \tag{4.5}$$

The integration is performed over the whole phase space of $\vec{x}$.
A description of the transfer functions used in this analysis can be found in Chapter 5.

4.2.2. Detector acceptance

The detector acceptance is the fraction of events that gets detected by the detector and passes the selection cuts.
An ideal detector with a solid angle of 4π and a perfect resolution would have an acceptance factor of 1.

But since the detector only covers a certain η range and requires certain conditions to be met to reconstruct an event properly (for example, a minimum ΔR distance between any two jets), not every event gets recognized by the detector.
This acceptance factor $A(\alpha)$ depends on the set of parameters – in this case, the top quark mass – and is combined with the total cross section to normalize the differential cross section.

$$\sigma_{acc} = A(\alpha) \cdot \sigma_{tot} \qquad . \tag{4.6}$$

4.3. The event likelihood

Combining Equations 4.5 and 4.6, the likelihood for a process to produce an event $\vec{y}$ inside the detector is

$$L(\vec{y}, \alpha) = \frac{\mathrm{d}\sigma_{obs}(\vec{y}, \alpha)}{\sigma_{acc}(\alpha)} \qquad .$$

α is a parameter or a set of parameters – for example, the top quark mass – which the process depends on.
For one event, multiple probabilities can be combined to a single event likelihood. This

can be used to include multiple processes, such as top quark pair production via gg-fusion or $q\bar{q}$-annihilation and a likelihood for background processes. The event likelihood for a number of processes, e.g. a signal likelihood and a background likelihood, can be combined by weighting them by their relative fraction of event f and adding them:

$$L_{evt}(\vec{y}, \alpha) = f \cdot L_{sig} + (1 - f) \cdot L_{bkg} \quad . \tag{4.7}$$

4.4. Parameter estimation

Equation 4.7 shows the likelihood of a single event. The combined likelihood for a set of events $\vec{y}_1, \ldots, \vec{y}_n$ is

$$L(\alpha) = \prod_{i=1}^{n} L_{evt}(\vec{y}_i, \alpha) \quad . \tag{4.8}$$

To estimate the parameters α, the maximum likelihood method is used: the best value for α is the one that maximizes the likelihood $L(\alpha)$. Usually, instead of maximizing the likelihood itself, one minimizes the negative logarithm of the likelihood,

$$-\ln L(\alpha) = \sum_{i=1}^{n} \ln L_{evt}(\vec{y}_i, \alpha) \quad .$$

This is mainly done for numerical stability when dealing with finite-precision floating point numbers on computers.

4.5. Application of the matrix element method in this analysis

This section discusses the application of the matrix element method in the measurement of the top quark mass in the ℓ+jets channel.

In this case, there is only one parameter to be estimated, $\alpha = m_t$.
There are two partons in the initial state and six particles in the final state: two b-jets, two light jets, a charged lepton and a neutrino.
Each of the event's eight particles has an index i associated to it to denote its four-momentum p_i, its momentum $\vec{p}_i$, its energy E_i etc.
The indices range from 0 to 7, with the order of the associated particles being:

0. the first incoming parton,
1. the second incoming parton,
2. the b-quark from the hadronic side,
3. the b-quark from the leptonic side,
4. the first light quark,
5. the second light quark,
6. the charged lepton,
7. the neutrino.

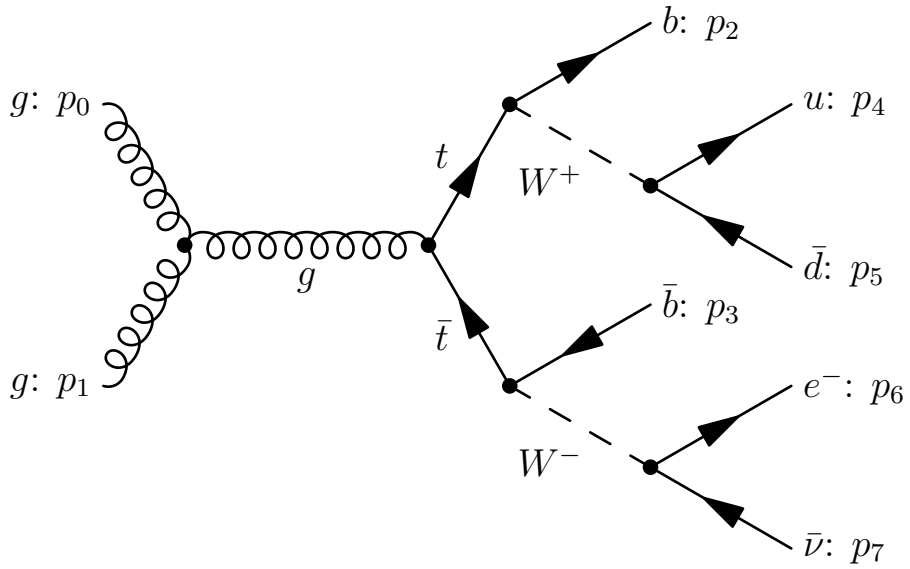

Figure 4.1.: Feynman diagram of $t\bar{t}$ production via gg-fusion and decay in the semileptonic channel with their associated labels.

The indices for each particle in the process are also shown in Figure 4.1.

The masses of all particles except for the b-quarks are negligible compared to their energies and will thus be assumed to be 0.

A computer programme has been developed by the author to compute the matrix element method's likelihoods. The programme is called **MEMTool** and will be described thoroughly in Chapter 6.

The analysis in this thesis is intended to serve as a preparation step for a full top quark

mass measurement. The plan for that measurement is to use two b-tags in the event selection, reducing the number of background events to a tiny fraction of the selected events. Therefore, this analysis does not make use of a background likelihood for its most common background process, W + jets. For the other major background, QCD, a matrix element is not even available.

As for the signal processes, only the matrix element for gluon-gluon fusion is used. This has been done to be able to better determine the programme's performance on the simulated parton level events in Chapter 7, which have been generated with gluon-gluon fusion as the only process, and because gg-fusion is the dominant process at a centre-of-mass energy of 7 TeV, accounting for most $t\bar{t}$ events.
MEMTool can be configured to also consider quark-antiquark annihilation processes without much effort; it already includes implementations for $q\bar{q}$ matrix elements.

Furthermore, only events where the charged lepton in the final state is an electron are considered.

To make the numerical integration over the whole phase space from Equation 4.5 feasible, the integration variables are changed and reduced from 20 to six. Also, a narrow width approximation is applied, resulting in a further reduction down to four dimensions. The details of this transformation are explained in Chapter 6.

The transfer functions used in this analysis are generated by a fit to ATLAS Mc10b Monte Carlo data. They are described in Chapter 5.

5. The transfer functions

The total transfer function used in the likelihood calculation (Equation 4.5) can be split up into a product of single transfer functions for each particle,

$$W(\vec{x}, \vec{y}) = W_{jet}(x_1, y_1) \cdot W_{lep}(x_2, y_2) \dots \quad , \tag{5.1}$$

which in turn can be split up into transfer functions for the particle's energy E and its angular coordinates ϕ and η.

The transfer functions shown in this chapter are probability distributions. They describe the probability that a particle with a real energy of E_{truth} is measured in the detector with an energy of E_{reco}.
The other two dimensions which can be treated with transfer functions are the azimuthal angle ϕ and the pseudorapidity η. However, because of the excellent angular resolution of the ATLAS detector, these two quantities are measured so precisely that they are assumed to be exact, or, in terms of transfer functions:

$$W_\phi(\phi_{reco}, \phi_{truth}) = \delta(\phi_{reco} - \phi_{truth}) \quad , \tag{5.2}$$

$$W_\eta(\eta_{reco}, \eta_{truth}) = \delta(\eta_{reco} - \eta_{truth}) \quad . \tag{5.3}$$

Two sets of transfer functions are used in this thesis: The first one consists of Gaussian distributions. The second one has sums of two Gaussians as probability distribution, with their parameters fitted to match ATLAS Mc10b Monte Carlo data.

These transfer functions do not apply to neutrinos, as they are not detected by the detector.

5.1. Gaussian transfer functions

The motivation for the first set of transfer functions comes from the detector design [33], which gives the energy resolution of the electromagnetic and hadronic calorimeters in

terms of standard deviations that increases with $\sqrt{E}$ (see Equations 3.1 and 3.2). Therefore, this set of transfer functions uses Gaussian distributions,

$$W(E_{reco}, E_{truth}) = \frac{1}{\sigma\sqrt{2\pi}} \cdot \exp\left(-\frac{1}{2}\left(\frac{E_{reco} - E_{truth}}{\sigma}\right)^2\right) \quad .$$

The standard deviation σ is different for jets and leptons.
For jets, it is

$$\sigma_{jet} = 0.5 \cdot \sqrt{E_{reco}} \quad ,$$

while leptons have the smaller standard deviation of

$$\sigma_{lepton} = 0.1 \cdot \sqrt{E_{reco}} \quad .$$

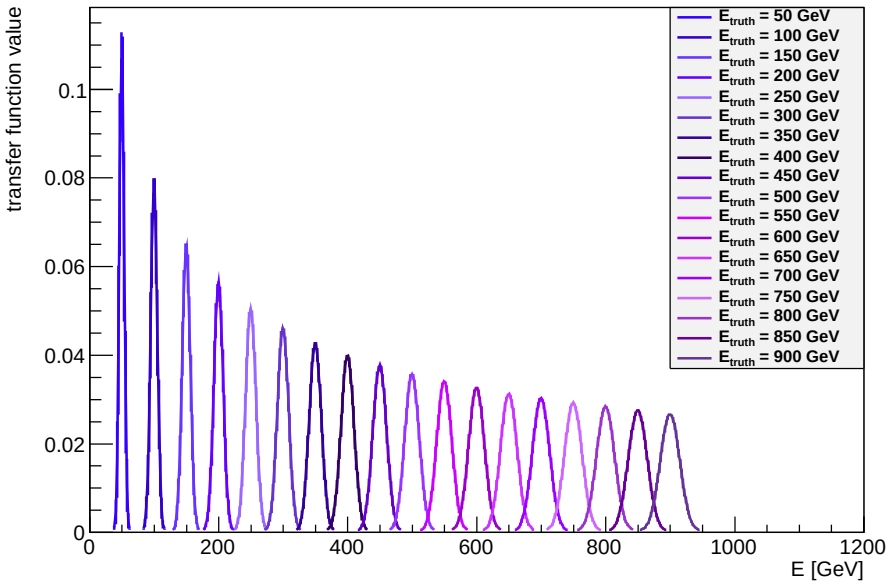

Figure 5.1.: Gaussian transfer function for jets for different energies.

Plots of the transfer functions for jets and leptons for a range of energies between 50 GeV and 900 GeV are shown in Figures 5.1 and 5.2, respectively.

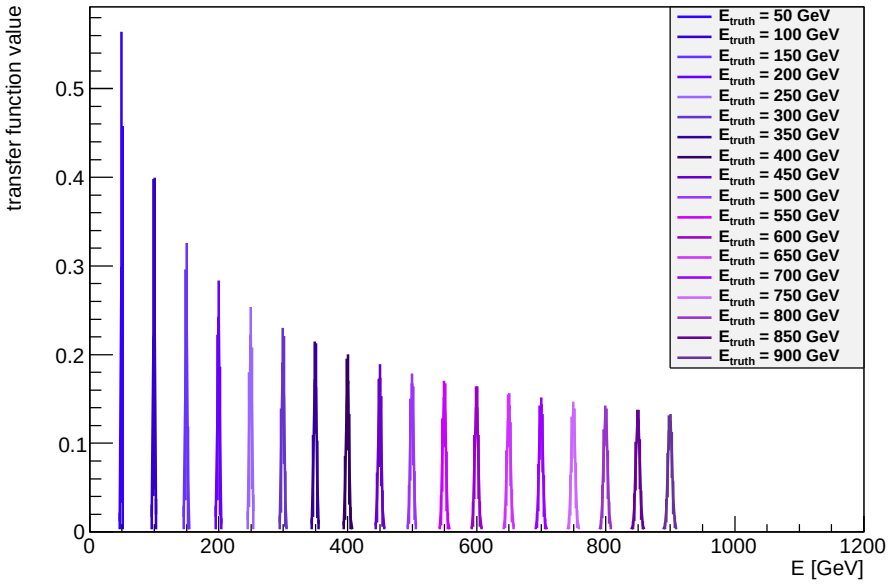

Figure 5.2.: Gaussian transfer function for leptons for different energies.

5.2. Mc10b transfer functions

Though the detector is designed to have these Gaussian transfer functions, the actual detector response is slightly different, asymmetric, and dependent on η. The η-dependency occurs because particles with a high $|\eta|$ pass more detector material than particles with a low $|\eta|$.
For a better approximation of the real detector response, this set of transfer functions is modelled with a combination of two Gaussians,

$$W\left(x := \frac{E_{truth} - E_{reco}}{E_{truth}}; \mu_1, \sigma_1, \omega, \mu_2, \sigma_2\right) = \frac{1}{(\sigma_1 + \omega\sigma_2)E_{truth}\sqrt{2\pi}} \left(\exp\left(-\frac{1}{2}\left(\frac{x-\mu_1}{\sigma_1}\right)^2\right) + \omega \cdot \exp\left(-\frac{1}{2}\left(\frac{x-\mu_2}{\sigma_2}\right)^2\right)\right) \quad .$$

The definition of the parameters μ_1, σ_1, ω, μ_2 and σ_2 differ for each type of particle (light jets, b-jets, electrons and muons) in order to better fit their respective energy dependency.
The values for the parameters have been optimised using the programme `KLFitter` to best fit the detector response simulated in ATLAS Mc10b Monte Carlo events [35].

5.2.1. Transfer function for light jets

The transfer function's parameters for light jets are:

$$\begin{aligned}
\sigma_1 &= \Theta\left(\frac{p_3}{\sqrt{E_{truth}}} + p_4\right) \\
\mu_1 &= \Theta\left(p_1 + E_{truth} \cdot p_2\right) \\
\omega &= \Theta\left(p_5 + E_{truth} \cdot p_6\right) \\
\mu_2 &= \Theta\left(p_7 + E_{truth} \cdot p_8\right) \\
\sigma_2 &= \Theta\left(p_9 + E_{truth} \cdot p_{10}\right)
\end{aligned}$$

Here, $\Theta(x)$ is defined as a step function that returns x if x is positive and 0 otherwise:

$$\Theta(x) = \begin{cases} 0: & x < 0 \\ x: & x \geq 0 \end{cases}$$

The values for $p_1, \ldots p_{10}$ are dependent on η. Their values are shown in Table 5.1.
A plot of the light jet transfer function for different energies is shown in Figure 5.3.

parameter	parameter value for η regions				
	$\lvert\eta\rvert \leq 0.8$	$0.8 < \lvert\eta\rvert \leq 1.37$	$1.37 < \lvert\eta\rvert \leq 1.52$	$1.52 < \lvert\eta\rvert \leq 2.5$	$2.5 < \lvert\eta\rvert \leq 4.5$
p_1	-0.0455	$-0.047\,62$	$-0.039\,78$	$-0.048\,36$	-0.3679
p_2	$1.013 \cdot 10^{-4}$	$5.546 \cdot 10^{-5}$	$9.214 \cdot 10^{-5}$	$1.138 \cdot 10^{-4}$	$1.244 \cdot 10^{-3}$
p_3	1.119	1.407	1.471	1.327	-2.756
p_4	$0.025\,24$	$6.649 \cdot 10^{-3}$	$0.020\,57$	$0.025\,81$	0.4537
p_5	0.136	0.2722	0.2855	0.6945	-3.16
p_6	$4.685 \cdot 10^{-5}$	$-7.768 \cdot 10^{-4}$	$-8.845 \cdot 10^{-4}$	$-1.618 \cdot 10^{-3}$	$0.030\,75$
p_7	$0.019\,98$	-0.1261	-0.1804	-0.1233	$0.016\,96$
p_8	$5.32 \cdot 10^{-5}$	$1.057 \cdot 10^{-3}$	$1.21 \cdot 10^{-3}$	$7.504 \cdot 10^{-4}$	$4.189 \cdot 10^{-5}$
p_9	0.3336	0.3385	0.3431	0.2723	0.1536
p_{10}	$-3.1165 \cdot 10^{-4}$	$-4.225 \cdot 10^{-4}$	$-1.929 \cdot 10^{-4}$	$-1.365 \cdot 10^{-4}$	$1.871 \cdot 10^{-5}$

Table 5.1.: Fitted parameter values for light jets for all η regions.

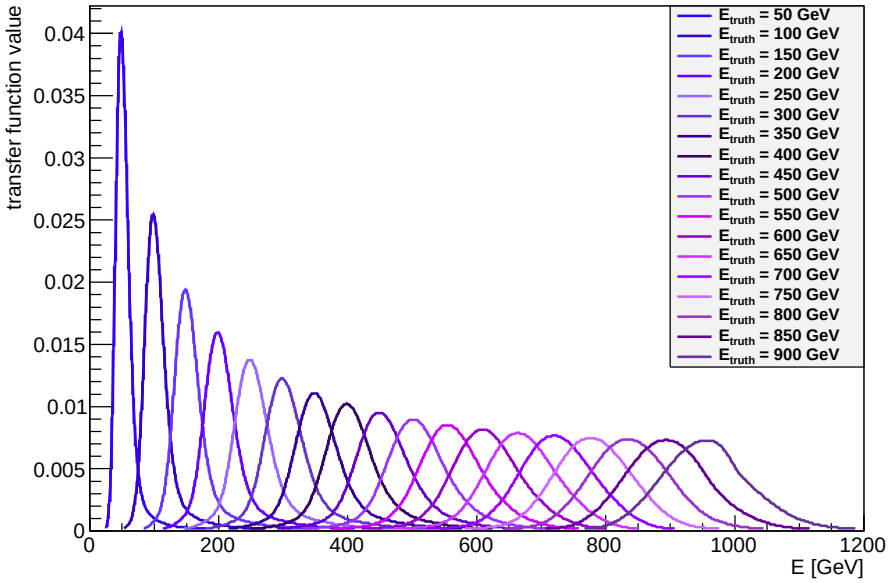

Figure 5.3.: Mc10b transfer function for light jets for different energies, in the region $|\eta| < 0.8$.

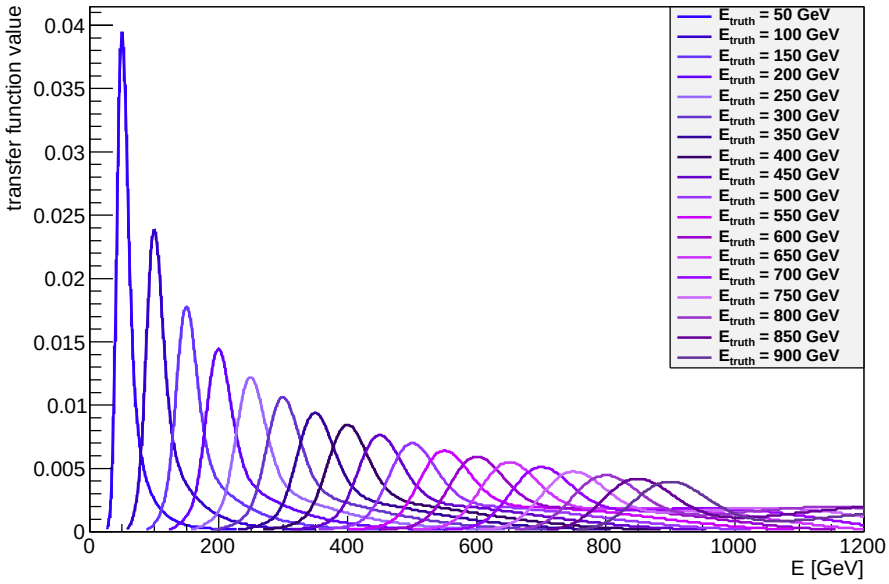

Figure 5.4.: Mc10b transfer function for b-jets for different energies, in the region $|\eta| < 0.8$.

parameter	parameter value for η regions				
	$\lvert\eta\rvert \leq 0.8$	$0.8 < \lvert\eta\rvert \leq 1.37$	$1.37 < \lvert\eta\rvert \leq 1.52$	$1.52 < \lvert\eta\rvert \leq 2.5$	$2.5 < \lvert\eta\rvert \leq 4.5$
p_1	0.1423	0.0826	0.2605	0.3645	1.023
p_2	$-4.497 \cdot 10^{-5}$	$-3.971 \cdot 10^{-5}$	$-2.845 \cdot 10^{-5}$	$-3.299 \cdot 10^{-5}$	$1.404 \cdot 10^{-4}$
p_3	0.8136	1.005	1.741	1.011	−1.708
p_4	0.035 18	0.023 46	−0.019 89	0.037 46	0.2785
p_5	4.339	8.023	7.689	12.56	5.302
p_6	$3.675 \cdot 10^{-4}$	$-7.728 \cdot 10^{-4}$	$-3.75 \cdot 10^{-4}$	$-9.417 \cdot 10^{-4}$	$-6.653 \cdot 10^{-4}$
p_7	0.087 63	0.074 06	0.054 31	0.047 66	−0.5094
p_8	$1.819 \cdot 10^{-4}$	$2.357 \cdot 10^{-4}$	$2.72 \cdot 10^{-4}$	$3.851 \cdot 10^{-4}$	$2.147 \cdot 10^{-3}$
p_9	0.2787	0.2583	0.3005	0.254	0.1269
p_{10}	$-1.77 \cdot 10^{-4}$	$-7.056 \cdot 10^{-5}$	$-2.533 \cdot 10^{-4}$	$-5.504 \cdot 10^{-5}$	$7.677 \cdot 10^{-4}$

Table 5.2.: Fitted parameter values for b-jets for all η regions.

5.2.2. Transfer function for b-jets

The transfer function's parameters for b-jets are:

$$\begin{aligned}
\mu_1 &= \Theta\left(p_1 + E_{truth} \cdot p_2\right) \\
\sigma_1 &= \Theta\left(\frac{p_3}{\sqrt{E_{truth}}} + p_4\right) \\
\omega &= \Theta\left(p_5 + E_{truth} \cdot p_6\right) \\
\mu_2 &= \Theta\left(p_7 + E_{truth} \cdot p_8\right) \\
\sigma_2 &= \Theta\left(p_9 + E_{truth} \cdot p_{10}\right)
\end{aligned}$$

The values for $p_1, \ldots p_{10}$ are dependent on η. Their values are shown in Table 5.2. A plot of the b-jet transfer function for different energies is shown in Figure 5.4.

5.2.3. Transfer function for electrons

The transfer function's parameters for electrons are:

$$\begin{aligned}
\mu_1 &= \Theta\left(p_1 + E_{truth} \cdot p_2\right) \\
\sigma_1 &= \Theta\left(\frac{p_3}{\sqrt{E_{truth}}} + p_4\right) \\
\omega &= \Theta\left(p_5 + E_{truth} \cdot p_6\right) \\
\mu_2 &= \Theta\left(p_7 + E_{truth} \cdot p_8\right) \\
\sigma_2 &= \Theta\left(p_9 + E_{truth} \cdot p_{10}\right)
\end{aligned}$$

The values for $p_1, \ldots p_{10}$ are dependent on η. Their values are shown in Table 5.3. A plot of the electron transfer function for different energies is shown in Figure 5.5.

parameter	parameter value for η regions		
	$\lvert\eta\rvert \leq 0.8$	$0.8 < \lvert\eta\rvert \leq 1.37$	$1.52 < \lvert\eta\rvert \leq 2.5$
p_1	$3.437 \cdot 10^{-3}$	$8.416 \cdot 10^{-3}$	$1.174 \cdot 10^{-3}$
p_2	$-2.57 \cdot 10^{-6}$	$-2.99 \cdot 10^{-5}$	$1.8 \cdot 10^{-5}$
p_3	0.041 63	0.1977	0.1097
p_4	0.012 34	$2.103 \cdot 10^{-3}$	0.011 19
p_5	0.061 43	0.1217	0.353
p_6	$-7.19 \cdot 10^{-5}$	$-4.727 \cdot 10^{-4}$	$-11.028 \cdot 10^{-3}$
p_7	0.032 88	0.062 86	0.065 61
p_8	$9.926 \cdot 10^{-5}$	$-1.86 \cdot 10^{-4}$	$-1.462 \cdot 10^{-4}$
p_9	0.037 97	0.054 35	0.067 11
p_{10}	$2.145 \cdot 10^{-4}$	$-2.652 \cdot 10^{-5}$	$-1.035 \cdot 10^{-5}$

Table 5.3.: Fitted parameter values for electrons for all η regions.

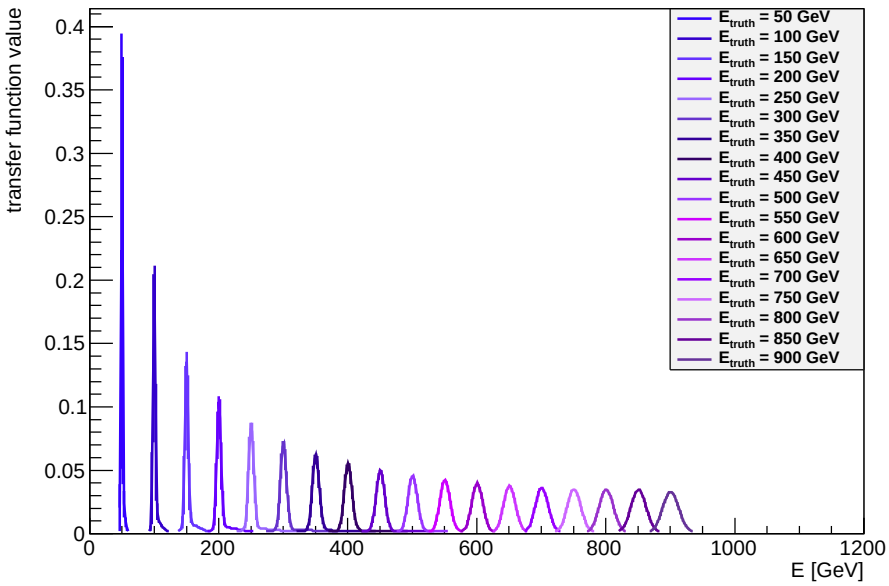

Figure 5.5.: Mc10b transfer function for electrons for different energies, in the region $|\eta| < 0.8$.

5.2.4. Transfer function for muons

The transfer function's parameters for muons are:

$$\begin{aligned}
\mu_1 &= \Theta\left(p_1 + E_{truth} \cdot p_2\right) \\
\sigma_1 &= \Theta\left(p_3 + E_{truth} \cdot p_4\right) \\
\omega &= \Theta\left(p_5 + E_{truth} \cdot p_6\right) \\
\mu_2 &= \Theta\left(p_7 + E_{truth} \cdot p_8\right) \\
\sigma_2 &= \Theta\left(p_9 + E_{truth} \cdot p_{10}\right)
\end{aligned}$$

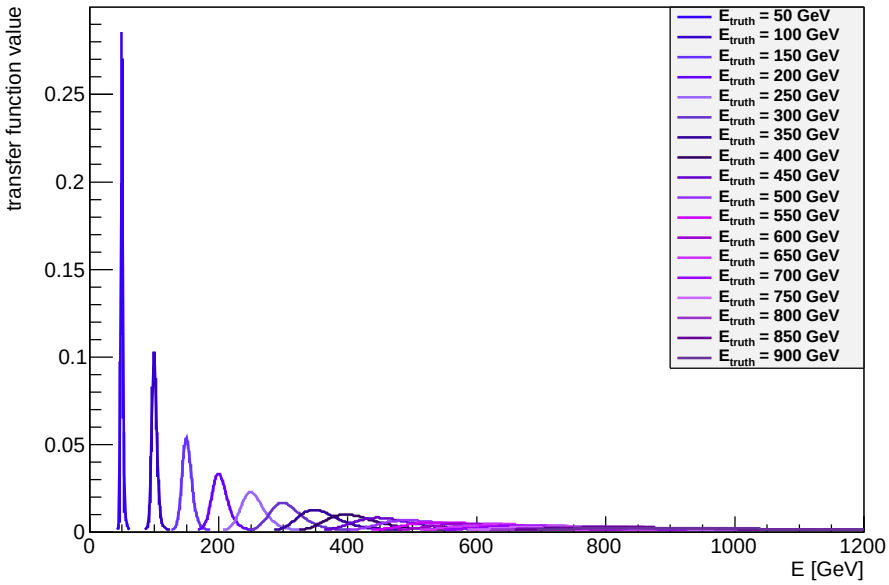

Figure 5.6.: Mc10b transfer function for muons for different energies, in the region $|\eta| < 0.8$.

The values for $p_1, \ldots p_{10}$ are dependent on η. Their values are shown in Table 5.4.
A plot of the muon transfer function for different energies is shown in Figure 5.6.

parameter	parameter value for η regions		
	$\lvert\eta\rvert \leq 0.8$	$0.8 < \lvert\eta\rvert \leq 1.37$	$1.52 < \lvert\eta\rvert \leq 2.5$
p_1	$-2.594 \cdot 10^{-4}$	$7.124 \cdot 10^{-4}$	$-2.45 \cdot 10^{-3}$
p_2	$2.688 \cdot 10^{-5}$	$2.876 \cdot 10^{-5}$	$6.758 \cdot 10^{-5}$
p_3	0.0162	0.018 79	0.027 02
p_4	$1.879 \cdot 10^{-4}$	$3.442 \cdot 10^{-4}$	$2.335 \cdot 10^{-4}$
p_5	0.017 78	$6.506 \cdot 10^{-3}$	0.016 39
p_6	$6.21 \cdot 10^{-4}$	$3.425 \cdot 10^{-4}$	$6.06 \cdot 10^{-4}$
p_7	0.043	0.1846	0.053 27
p_8	$-2.88 \cdot 10^{-4}$	$-2.187 \cdot 10^{-3}$	$-4.296 \cdot 10^{-4}$
p_9	0.062 78	0.1323	0.070 49
p_{10}	$2.101 \cdot 10^{-4}$	$-3.159 \cdot 10^{-4}$	$4.137 \cdot 10^{-4}$

Table 5.4.: Fitted parameter values for muons for all η regions.

6. MEMTool

MEMTool is a computer programme, written as a part of this thesis, for measuring the top quark mass in the semileptonic channel with the matrix element method.
It is written in C++ and is available from the ATLAS SVN server at [36].

MEMTool can calculate event likelihoods, combine likelihoods from multiple events and extract the top quark mass. It is also capable of generating calibration curves and performing ensemble testing.

MEMTool is modular in the sense that it has components – matrix elements, transfer functions, PDFs and sets of integration variables – which can easily be exchanged or extended.

This chapter will describe the programme with its components, show the available implementations for each component and explain the process of numerical integration that is used to integrate over the phase space.
User documentation and a class reference documentation are provided with MEMTool.

6.1. Details of the integration process

The main effort in the matrix element method is the computation of the event likelihood for a range of top quark masses. This integration cannot be performed analytically; instead, numerical integration techniques are used. MEMTool uses the VEGAS algorithm by Lepage, a Monte Carlo integration algorithm [37, 38].
It is not known unambiguously which of the four jets corresponds to which of the final state partons. Since two b-tags are required for the event selection, it is known which two jets have to be associated with the b-quarks. Counting in the fact that the used matrix element is symmetrical under the permutation of the light jet associations, there are only two possible jet/parton associations left. MEMTool computes the likelihood for both permutations separately and then averages over both results. This introduces a

combinatorial background, whose effects are shown in Chapter 7.
If not explicitely stated otherwise, all likelihood distributions shown below are the averaged results of both possible permutations.

6.1.1. Numerical integration with VEGAS

VEGAS estimates the integral

$$I = \int_\Omega f(\vec{x}) \mathrm{d}\vec{x}$$

of a function $f(\vec{x})$ over a volume Ω by computing the integrand at N random points $\vec{x}_i \in \Omega$ and forming the weighted average

$$I \approx S = \frac{1}{N} \sum_{i=1}^{N} \frac{f(\vec{x}_i)}{p(\vec{x}_i)} \quad .$$

The random points are chosen with a probability density $p(\vec{x})$. VEGAS makes m estimates $S_\lambda, \lambda = 1, \ldots, m$ of this integral, each using N evaluations. These m estimates are combined to give a cumulative estimate $\bar{S}$,

$$I \approx \bar{S} = \bar{\sigma}^2 \sum_{\lambda=1}^{m} \frac{S_\lambda}{\sigma_\lambda^2} \quad ,$$

where σ_λ is the approximate uncertainty in S_λ:

$$\sigma_\lambda^2 = \frac{1}{N(N-1)} \sum_{i=1}^{N} \frac{f(\vec{x}_i)^2}{p(\vec{x}_i)} - S_\lambda^2 \quad ,$$

and $\bar{\sigma}$ is the approximate uncertainty in $\bar{S}$:

$$\frac{1}{\bar{\sigma}^2} = \sum_{\lambda=1}^{m} \frac{1}{\sigma_\lambda^2} \quad .$$

VEGAS also determines whether the various estimates are consistent by computing the χ^2 per degree of freedom or not.

The simplest Monte Carlo integration algorithms use a uniform distribution for sampling random integration points, i.e. $p(\vec{x}) = \text{const.}$.
In VEGAS, $p(\vec{x})$ is modified so as to minimize σ_λ^2. Uniformly distributed points are used in the first iteration of the integration algorithm. The information gained about $f(\vec{x})$

in this first sampling is then used to define a new density $p'(\vec{x})$ which reduces σ_λ^2 in the next iteration. After each subsequent iteration, $p(\vec{x})$ is again refined for use in the next, gradually reducing σ_λ^2 and improving the estimate $\bar{S}$.

In theory, σ_λ^2 is minimized when

$$p(\vec{x}) = \frac{|f(\vec{x})|}{\int_\Omega |f(\vec{x})| \mathrm{d}x} \quad ,$$

which means that more sample points are chosen from regions where the integrand has the largest magnitude. VEGAS tries to approximate this ideal by dividing the integration volume into a grid of hypercubes. Random points are distributed so that the average number of points per hypercube is the same. After each iteration, the increment sizes of the axes are adjusted in order to concentrate hypercubes in the regions where $|f(\vec{x})|$ is largest, until the optimal grid is obtained.

Instead of relying on a custom implementation, MEMTool uses the fast and stable VEGAS methods from the GNU Scientific Library [39].

6.1.2. Integration variables and phase space transformations

The integration in Equation 4.5 is performed over the whole phase space, which means 24 dimensions, 6 (3×2) for the momenta of the initial state particles and 18 (3×6) for the momenta of the final state particles.
This number, which is unfeasible in terms of integration dimensions, can be reduced to 20 by assuming that the x- and y- momenta of the initial particles be 0. This assumption is reasonable as the initial particles travel along the direction of the beam pipe. Now, the initial partons' four-momenta are fully defined by their respective fraction of the incoming protons' energies, x_1 and x_2:

$$E_0 = x_1 \cdot 3500 \text{ GeV} \quad ; \quad \vec{p}_0 = \begin{pmatrix} 0 \\ 0 \\ x_1 \end{pmatrix} \cdot 3500 \text{ GeV}$$

$$E_1 = x_2 \cdot 3500 \text{ GeV} \quad ; \quad \vec{p}_1 = -\begin{pmatrix} 0 \\ 0 \\ x_2 \end{pmatrix} \cdot 3500 \text{ GeV}$$

Furthermore, the integral contains four δ distributions for the conservation of energy and momentum, which effectively reduce the number of dimensions from 20 to 16. They are usually used to fix the values of x_1, x_2, p_7^x and p_7^y.
With the assumption that η and ϕ are measured precisely (see Equations 5.2 and 5.3), 10 more variables are fixed – two for each outgoing particle except the neutrino – which reduces the number of integration variables down to 6.

The remaining six integration variables should be chosen wisely. The simplest choice would be to integrate over the energies of all jets and the charged lepton as well as the neutrino's z-momentum. The downside of this choice is that the values for these variables, for which neither the matrix element nor the transfer functions make the integrand vanish, are sparse in this phase space. Therefore, choosing these integration variables requires a high number of integration points.
Variables that follow a known distribution, such as the masses of the W bosons and top quarks, are much better choices, as they let the integration algorithm converge much faster. They do, however, require a more sophisticated algorithm to calculate all particles' four-momenta from the integration variables.

Associated with each choice of integration variables is a different phase space volume element Φ_6.

6.2. MEMTool's components

6.2.1. Matrix elements

The base class for the matrix elements is `MEMTool::ME::ME`. It provides an interface for all matrix elements. A matrix element has a process (either gg or $q\bar{q}$) and is dependent on the top quark mass and width, and on the event's kinematic.

There are currently five implementations of matrix elements available: `MadGraphGGME`, `MadGraphQQME`, `KleissStirlingGGME`, `KleissStirlingQQME` and `NoCorrelationGGME`. All matrix element implementations reside in the namespace `MEMTool::ME`.

MadGraphGGME is a wrapper for the matrix element code generated with MadGraph 5 [40]. The process used for generation of the MadGraph code is

```
g g > t t~ > b b~ u d~ e- ve .
```

MadGraphQQME is, like `MadGraphGGME`, a wrapper for MadGraph-generated matrix element code, for the process

```
u d~ > t t~ > b b~ u d~ e- ve~ .
```

KleissStirlingGGME and KleissStirlingQQME are the $t\bar{t}$ matrix elements for gluon-gluon fusion and quark-antiquark annihilation, respectively, following the formulae given by Kleiss and Stirling in [41].
The analytical expression and the resulting code are relatively compact, while including both the effects of a finite width of the W bosons in the top quark decay and those of a non-zero b quark mass, as well as the complete spin correlation in the decays.

NoCorrelationGGME is the $t\bar{t}$ matrix element for gluon-gluon fusion used in [42, 43]. The matrix element does take spin correlations into account, resulting in the analytical expression for the amplitude,

$$|\mathcal{M}|^2 = \frac{g_s^4}{9} F \bar{F} (2 - \beta^2 \sin^2 \theta_{qt}) \quad ,$$

where g_s is the strong coupling constant and θ_{qt} describes the angle between the incoming partons in their rest frame and the top quark. The factors F and $\bar{F}$ describe the leptonic and hadronic decay of the top quark:

$$F = \frac{g_W^4}{4} \frac{\pi(m_t^2 - m_{W,lep}^2)}{m_t \Gamma_t} \frac{m_t^2(1 - c_{36}^2) + m_{W,lep}^2(1 + c_{36})^2}{(m_{W,lep}^2 - m_W^2)^2 + m_W^2 \Gamma_W^2} \quad \text{, and}$$
$$\bar{F} = \frac{g_W^4}{4} \frac{\pi(m_t^2 - m_{W,had}^2)}{m_t \Gamma_t} \frac{m_t^2(1 - c_{25}^2) + m_{W,had}^2(1 + c_{25}^2)}{(m_{W,had}^2 - m_W^2)^2 + m_W^2 \Gamma_W^2} \quad ,$$

where g_W is the weak coupling constant and c_{ij} is the cosine of the angle between particle i and particle j in their respecive rest frame.
This very compact matrix element is by far the fastest to compute.

6.2.2. Transfer functions

The base class for the transfer functions is `MEMTool::TF::TF`. It provides an interface with just one function, called `getTF()`, which takes the event and the current point in the phase space and returns the total combined transfer function $W(\vec{x}, \vec{y})$ from Equation 5.1.

There are currently three implementations of transfer functions in MEMTool within the namespace `MEMTool::TF`:

AlwaysOneTF is a trivial implementation of `TF` that – as the name suggests – always returns a value of 1. It is used only in combination with `DeltaKinematic`, described in Section 6.2.4.

GaussianTF is an implementation of the Gaussian transfer functions described in Section 5.1.

Mc10bTF is an implementation of the ATLAS Mc10b transfer functions described in Section 5.2.

6.2.3. Parton distribution functions

The base class for the PDFs is `MEMTool::PDF::PDF` and currently has two implementations in the namespace `MEMTool::PDF`.

LHAPDF is a wrapper to the LHAPDF library, which provides a unified and easy to use interface to many PDF sets. It can be configured to use any PDF set that LHAPDF supports by passing the PDF's name.
The default PDF choice used in this analysis is the leading order PDF CTEQ6l.

CachedLHAPDF is a caching version of the aforementioned LHAPDF class. The vast amount of calls to the LHAPDF library during integration requires a high computational effort. This computing time is reduced drastically by using this class, which creates a lookup table for the PDF values with $100,000$ entries upon construction and uses this lookup table instead of calling the LHAPDF library.
For increased precision, a linear interpolation between lookup values is also done.

6.2.4. Integration variables

These classes handle different sets of integration variables, the corresponding phase space volume element and the algorithm to calculate all particle's four-momenta from the integration variables discussed in Section 6.1.2.
They all inherit from `MEMTool::Kinematic::Kinematic` and reside in the namespace `MEMTool::Kinematic`.

SimplePznuKinematic is a `Kinematic` implementation that uses five energies and the neutrino's z-momentum as integration variables.
Its six integration variables are:

- E_2, the energy of the first b-jet,
- E_3, the energy of the second b-jet,
- E_4, the energy of the first light jet,
- E_5, the energy of the second light jet,
- E_6, the energy of the charged lepton, and
- p_7^z, the neutrino's z-momentum.

All angles (η and ϕ) are assumed to be exact.

Its phase space volume element, without the δ distributions, is

$$\mathrm{d}\Phi_6 = \prod_{i=2}^{6} \frac{|\vec{p}_i| \mathrm{d}E_i}{2(2\pi)^3} \cdot \frac{\mathrm{d}p_7^z}{2(2\pi)^3 E_7} \quad . \tag{6.1}$$

The kinematic reconstruction for this set of integration variables can be found in Appendix A.1.

DeltaKinematic is a `Kinematic` implementation which is used for testing on unsmeared parton-level events. It has only one integration variable: the neutrino's z-momentum p_7^z; all other momenta are taken to be precise. The neutrinos x- and y-momentum, as well as the incoming partons' energy fractions (x_1 and x_2 in Equation 4.3) are calculated from the constraints set by the conservation of energy and momentum.
`DeltaKinematic` is used in conjunction with `AlwaysOneTF`, which is described in Section 6.2.2.
Its phase space volume element is the same as the one in Equation 6.1.

WmassKinematic is a `Kinematic` implementation that uses five energies and the mass of the leptonic W boson as integration variables.
Its six integration variables are:

- E_2, the energy of the first b-jet,
- E_3, the energy of the second b-jet,

- E_4, the energy of the first light jet,
- E_5, the energy of the second light jet,
- E_6, the energy of the charged lepton, and
- $m^2_{W,lep}$, the squared mass of the leptonic W boson.

This set of integration variables can have up to two valid solutions per integration point, as each W mass corresponds to two possible values for p_7^z with opposite sign.
Its phase space volume element, without the δ distributions, is

$$\mathrm{d}\Phi_6 = \prod_{i=2}^{6} \frac{|\vec{p}_i|\mathrm{d}E_i}{2(2\pi)^3} \cdot \frac{\mathrm{d}m^2_{W,lep}}{2(2\pi)^3 \left| E_6 \frac{p_7^z}{E_7} - p_6^z \right|} \quad .$$

The kinematic reconstruction can be found in Appendix A.2.

FourMassesKinematic is a `Kinematic` implementation which uses the two top quark masses, the two W boson masses and two energies as integration variables.
Its six integration variables are:

- E_4, the energy of the first light jet,
- E_6, the energy of the charged lepton,
- $m^2_{W,had}$, the squared mass of the hadronic W boson,
- $m^2_{W,lep}$, the squared mass of the leptonic W boson,
- $m^2_{t,had}$, the squared mass of the hadronic top quark, and
- $m^2_{t,lep}$, the squared mass of the leptonic top quark.

This set of integration variables can have up to four valid solutions per integration point.
Its phase space volume element, without the δ distributions, is

$$\begin{aligned}\mathrm{d}\Phi_6 = {} & \frac{\mathrm{d}E_4 \mathrm{d}E_6}{2(2\pi)^3 p_7^z} \cdot \prod_{i=2}^{6} \frac{|\vec{p}_i|^2}{2(2\pi)^3} \\ & \times \frac{\mathrm{d}m^2_{W,had}}{2E_4|1-\cos\theta_{45}|} \cdot \frac{\mathrm{d}m^2_{t,had}}{2\left|(E_4+E_5)\frac{|\vec{p}_2|}{E_2} - E_4\cdot\cos\theta_{42} - E_2\cdot\cos\theta_{52}\right|} \\ & \times \frac{\mathrm{d}m^2_{W,lep}}{2\left|E_6\frac{p_7^z}{E_7} - p_6^z\right|} \cdot \frac{\mathrm{d}m^2_{t,lep}}{2\left|(E_6+E_7)\frac{|\vec{p}_3|}{E_3} - E_6\cdot\cos\theta_{63} - E_3\cdot\cos\theta_{73}\right|} \quad ,\end{aligned}$$

where θ_{ij} is the angle between particle i and particle j.
The kinematic reconstruction for this set of integration variables is rather lengthy and computationally expensive, as it involves an iterative approximation approach and the solving of a fourth degree polynomial. The procedure can be found in Appendix A.3.

FourMassesNwaKinematic is a version of `FourMassesKinematic` that uses a narrow width approximation on the top quark masses to reduce the number of integration variables from six to four.
In this approximation, both the hadronic and the leptonic top quarks' masses are set to the current top quark mass hypothesis that is being tested. This is acceptable because of the small width of the top quark's small decay width.
Its phase space volume element is the same as the one for the `FourMassesKinematic`, but multiplied with a factor ρ to account for the narrow width approximation,

$$\rho = (\pi m_t \Gamma_t)^2$$

6.3. Default configuration

The default configuration for MEMTool is to use the `NoCorrelationGGME` matrix element, the `Mc10bTF` transfer functions, the `CachedLHAPDF` parton distribution functions and the integration variables defined by `FourMassesNwaKinematic`.

If not stated otherwise, the tests in the following chapters will use the aforementioned configuration.

7. Tests with simulated parton level events

To verify that MEMTool works correctly, it has to be tested. For this purpose, parton-level events for $t\bar{t}$ production via gluon-gluon fusion with subsequent semileptonic decay have been generated with MadEvent, using MadGraph's leading order matrix element [40]. Seven of these test samples are available, with input top quark masses of 160 GeV, 165 GeV, 170 GeV, 175 GeV, 180 GeV, 185 GeV and 190 GeV, respectively. The samples each contain 1000 simulated events.

Three tests have been carried out to ensure the proper functionality of MEMTool. The first test uses the unsmeared samples as input, without using transfer functions. For the second and third test, the effects of the transfer functions – Gaussian and Mc10b – were simulated by smearing the energies of the final state particles according to their transfer functions.

In this chapter, the results of these tests are presented.

As described in Section 4.2, the likelihoods have to be normalized with the total cross sections and the acceptance rates. Both depend only on the assumed top quark mass and not on the event. Therefore, they were calculated beforehand. The cross sections were calculated with MadGraph for each used top quark mass. The acceptance rates were calculated by generating $100,000$ events with MadGraph without any cuts for a set of top quark masses, cutting them manually and counting the remaining events. A second degree polynomial was fitted through the rates. The resulting acceptance rates are shown in Figure 7.1.

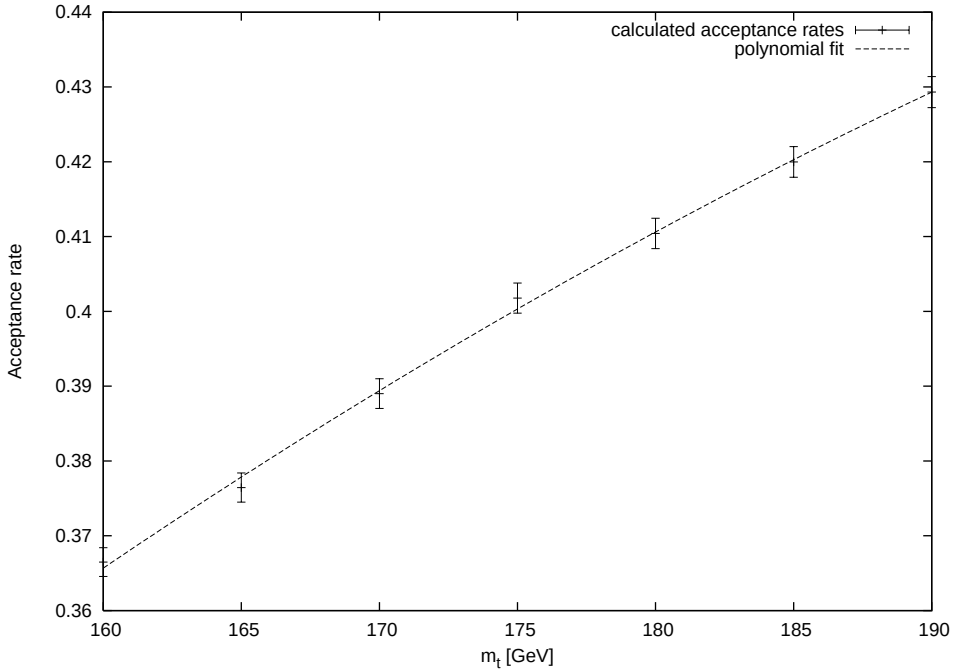

Figure 7.1.: Acceptance rates with a polynomial fit.

7.1. Results with unsmeared data

The first test is performed on unsmeared parton-level events. The energies of all final state particles – except for the neutrino – are considered to be precise, leaving the neutrino's z-momentum p_7^z as sole integration variable. Therefore, MEMTool was configured to use the combination of its modules `DeltaKinematic` and `AlwaysOneTF`.

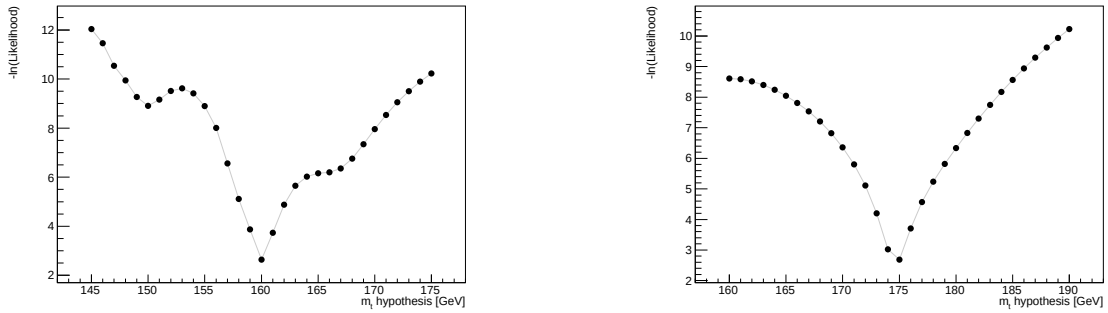

(a) single event likelihood with $m_t = 160$ GeV (b) single event likelihood with $m_t = 175$ GeV

Figure 7.2.: Single event likelihood distributions for (a) an event with input top quark mass 160 GeV and (b) an event with input top quark mass 175 GeV, using unsmeared data.

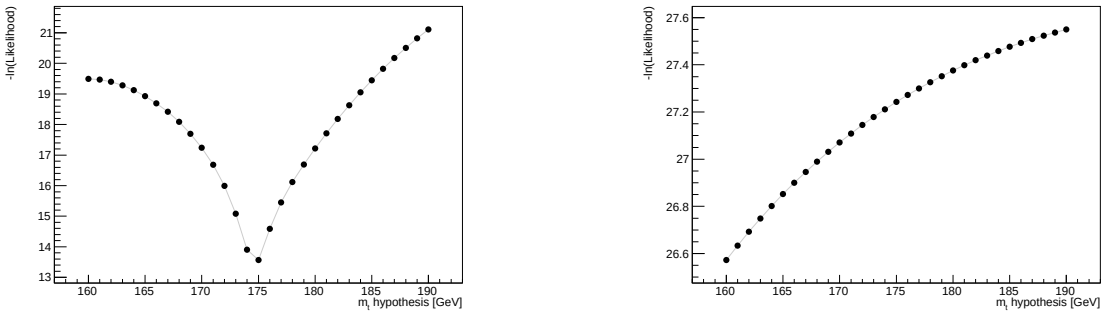

(a) right permutation (b) wrong permutation

Figure 7.3.: Single event likelihood distributions when using only one permutation of the possible jet/parton associations.

The resulting likelihoods generally have a sharp peak at their input mass, which can be seen for two example events in Figure 7.2. These results include combinatorial background from averaging over both the correct and the wrong jet/parton association. Figure 7.3(a) shows the likelihood when only the right permutation is used, Figure 7.3(b) shows the likelihood distribution that is the result of picking the wrong permutation. In this case, the wrong permutation has a much higher $-\ln(L)$ and thus only broadens the resulting likelihood distribution a bit when combined (Figure 7.2(b)).

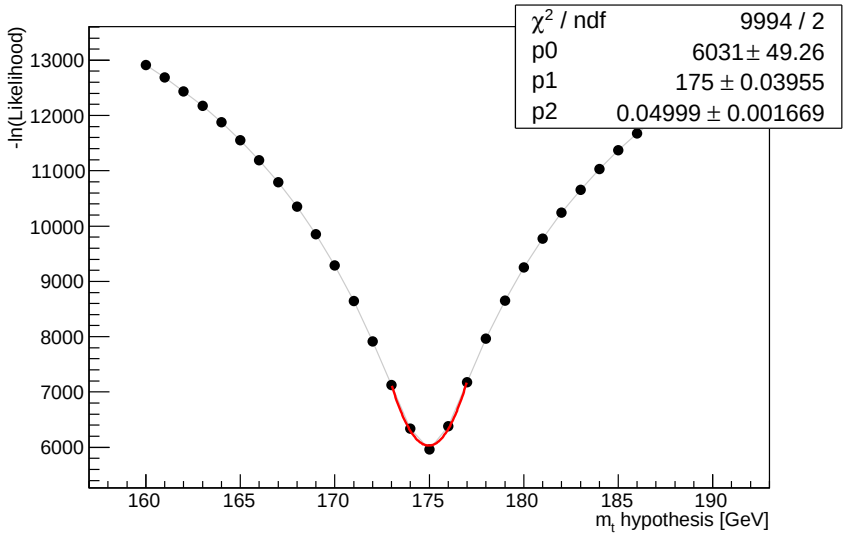

Figure 7.4.: Combined likelihood curve for 1000 events from the unsmeared sample with $m_t = 175$ GeV.

For each input top quark mass, the likelihood distribution for 1000 events has been computed and combined to a single likelihood distribution. The minimum and uncertainty have then been extracted from the combined likelihood distribution by fitting a parabola to the log-likelihood curve. The results for the $m_t = 175$ GeV sample can be seen in Figure 7.4. The fit yields an excellent result, returning a measured top quark mass of 175.00 ± 0.04 GeV.

Since the data samples were generated using a leading order matrix element and without any background process contributing to the data, the measured (output) top quark mass should always be equal to the input top quark mass. This behaviour can be seen in a calibration curve, where the output top quark mass is plotted against the input top quark mass[1]. A straight line is then fitted through the points, which should ideally have a slope of 1 and a y-intercept of 0. The calibration curve for this test, which is shown in Figure 7.5, has a slope of 1 and almost no shift. For comparison, the ideal calibration curve is shown by the dashed red line. This shows that for unsmeared data and without the use of transfer functions, MEMTool yields the correct results.

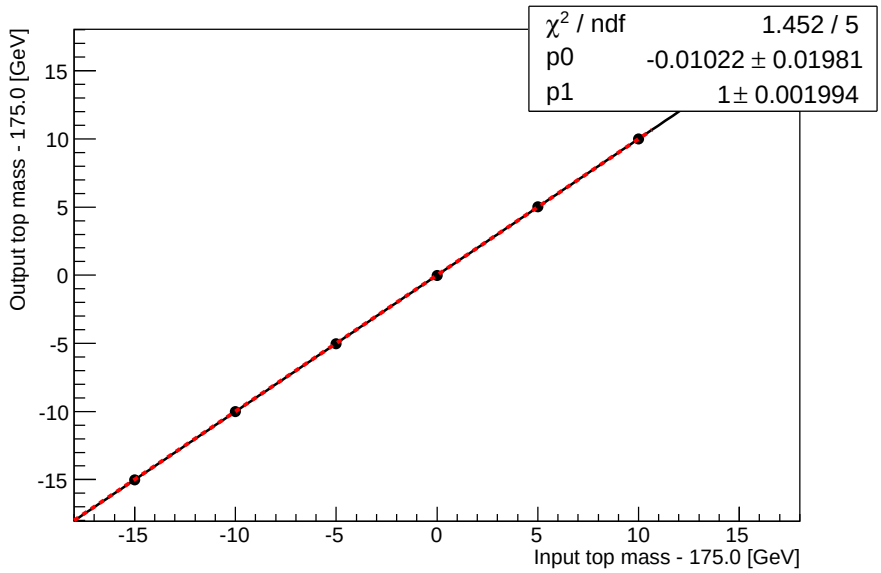

Figure 7.5.: Calibration curve for unsmeared parton level data.

[1] Actually, the plot shows both input and output top quark mass minus 175 GeV, so that the y-intercept of a straight line fitted through the points gives a better measure of the actual shift.

7.2. Results with Gaussian transfer functions

The second test shows the performance of MEMTool when using the Gaussian transfer functions. To generate suitable input data, the parton-level event samples were used: the final state particles' energies were randomly smeared according to their respective transfer functions by means of inverse transform sampling. To prevent unphysical events, the transfer functions were cut off so that the sampling could not result in negative energies for the smeared events.

An event selection is applied to the samples to select 1000 events from each sample. The selected events are required to have:

1. exactly four jets, all having $E > 20$ GeV and $\eta < 2.5$,
2. a b-tag for two of the jets,
3. exactly one electron with $E > 15$ GeV, and
4. $E_{T_{miss}} > 20$ GeV.

To identify the b-jets, the `JetFitterCOMBNN` b-tagger is used, which is a neural network-based combination of the JetFitter and IP3D b-tagging algorithms.

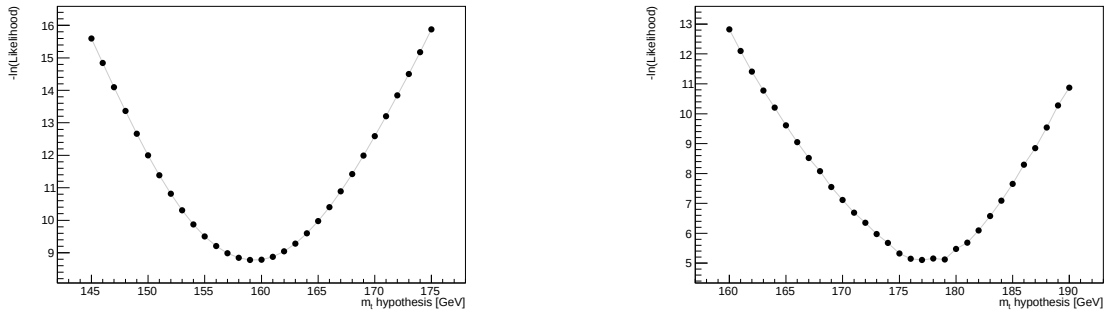

(a) single event likelihood with $m_t = 160$ GeV (b) single event likelihood with $m_t = 175$ GeV

Figure 7.6.: Single event likelihood distributions for (a) an event with input top quark mass 160 GeV and (b) an event with input top quark mass 175 GeV, using Gaussian transfer functions.

Figure 7.6 shows two single event likelihood distributions, which both have a much broader minimum due to the smearing and the use of transfer functions.

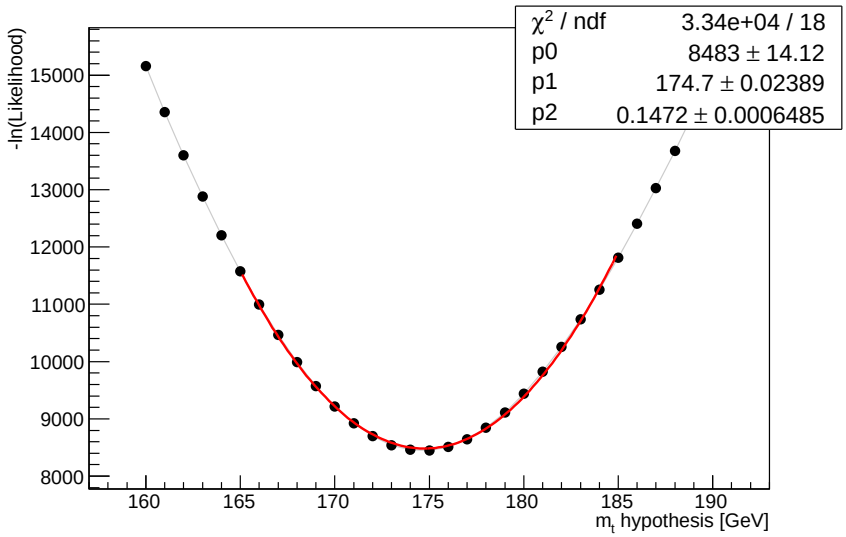

Figure 7.7.: Combined likelihood curve for 1000 events from the sample with $m_t = 175$ GeV using Gaussian transfer functions.

The combined likelihood distributions – as shown in Figure 7.7 for the $m_t = 175$ GeV sample – are also broader than without transfer functions, which is to be expected.

The calibration curve for this test is shown in Figure 7.8. The fitted line's slope is almost perfect; it has a small shift of 0.2255 GeV when compared to the ideal line, which is acceptable.

The consistency of the results is checked by using ensemble testing. 5000 ensembles are generated from each input sample by randomly selecting 100 events with replacement. For each ensemble, the combined likelihood distribution is generated and the top quark mass and its uncertainty is measured. From these values, a pull distribution is generated. The pull of an ensemble is defined as

$$p = \frac{m_{\text{ens}} - m_t}{\sigma_{\text{ens}}} \quad ,$$

where m_{ens} and σ_{ens} are the top quark mass and uncertainty extracted from the ensemble and m_t is the measured top quark mass for the whole sample. Ideally, for likelihood distributions that follow a Gaussian distribution, the pull distribution should fit a Gaussian distribution with mean $\mu = 0$ and standard deviation $\sigma = 1$. Since this is not the case, the pull distributions can only serve as an approximative hint whether the programme is work-

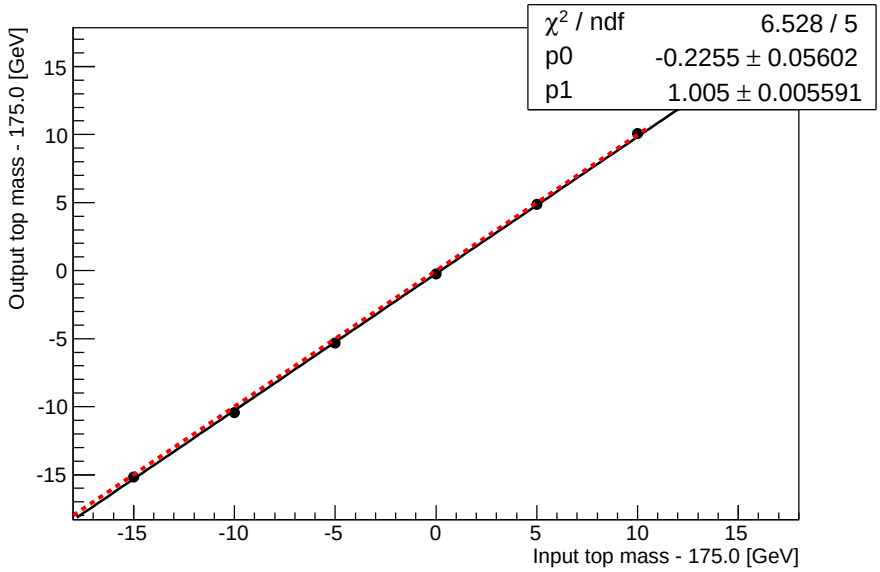

Figure 7.8.: Calibration curve for parton level data smeared with Gaussian transfer functions.

ing correctly. Figure 7.9 shows the pull distribution generated from the $m_t = 175$ GeV sample.

Figure 7.10 shows the mean and width of the pull distributions for all samples. The pull means are distributed around 0 and the widths around 1, which is a good indication that the method works correctly for Gaussian transfer functions. The pull width distribution in Figure 7.10(b) shows a possible trend to larger pull widths for higher top quark masses.

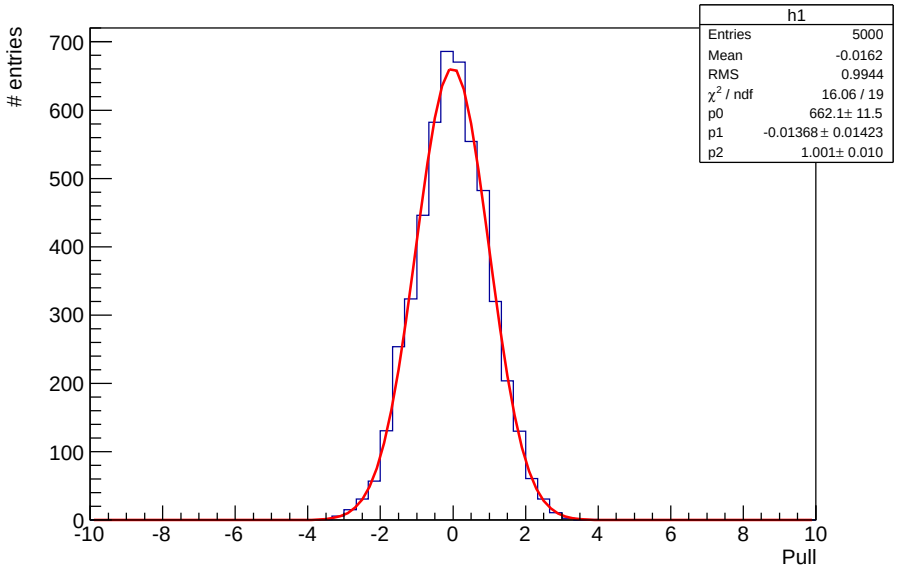

Figure 7.9.: Pull distribution with fitted Gaussian distribution for the $m_t = 175$ GeV sample with Gaussian transfer functions.

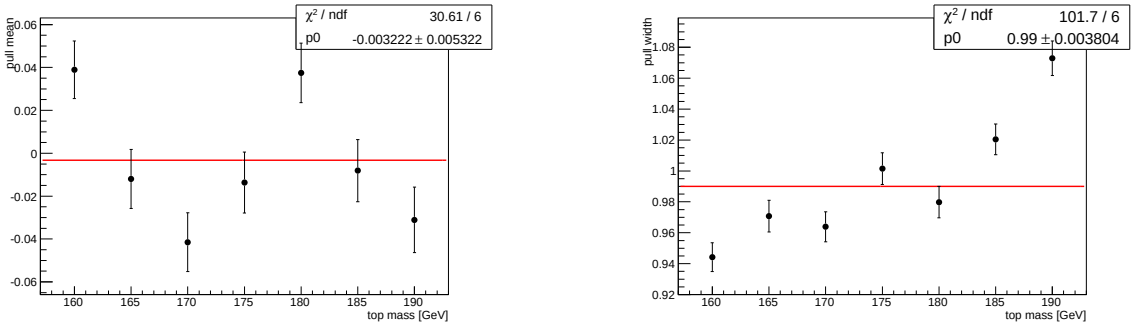

(a) pull mean

(b) pull width

Figure 7.10.: Pull mean and width for all samples with Gaussian transfer functions.

7.3. Results with Mc10b transfer functions

The input data for the test with Mc10b transfer functions was also generated from the parton-level event samples by smearing the energies according to their transfer functions' distributions. Again, the transfer functions were cut off for the inverse transform sampling in order to prevent negative energies. 1000 events were selected from each of the resulting samples, using the event selection from Section 7.2.

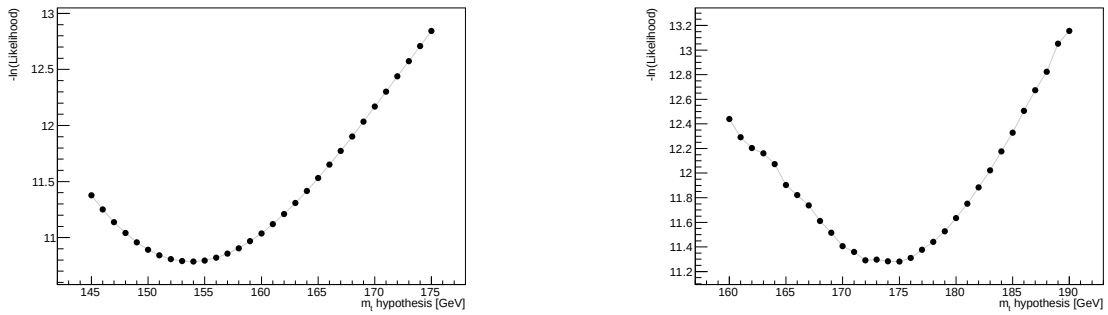

(a) single event likelihood with $m_t = 160$ GeV

(b) single event likelihood with $m_t = 175$ GeV

Figure 7.11.: Single event likelihood distributions for (a) an event with input top quark mass 160 GeV and (b) an event with input top quark mass 175 GeV, using Mc10b transfer functions.

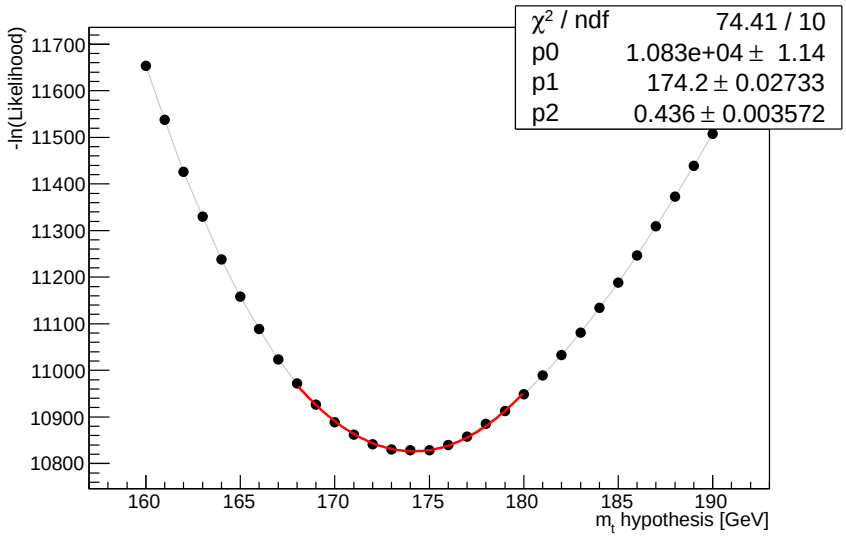

Figure 7.12.: Combined likelihood curve for 1000 events from the sample with $m_t = 175$ GeV using Mc10b transfer functions.

Figure 7.11 shows two single event likelihood distributions. The distributions are asymmetric and have wider peaks than the ones smeared with Gaussian transfer functions.

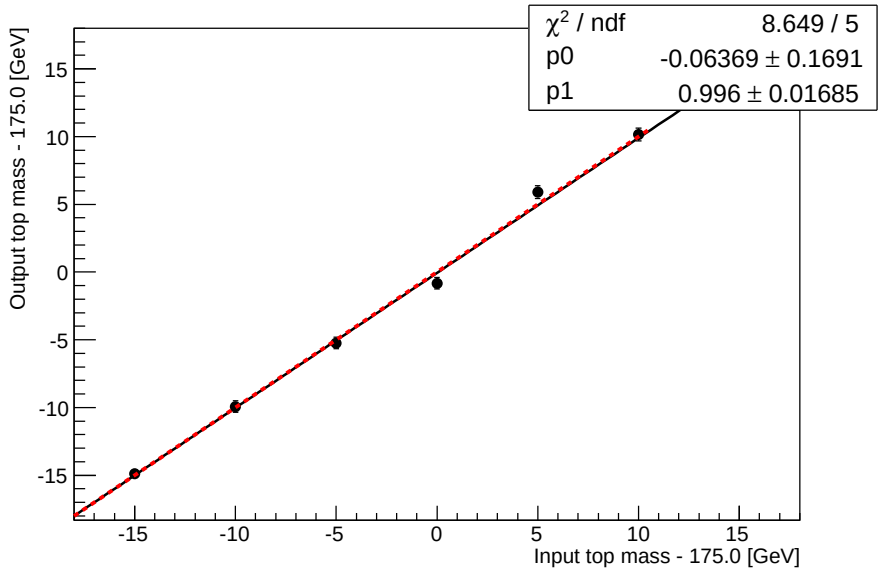

Figure 7.13.: Calibration curve for parton level data smeared with Mc10b transfer functions.

Figure 7.12 shows the combined likelihood distribution for $m_t = 175$ GeV. Most of the shifts and asymmetries, like the ones in Figure 7.11, cancel each other out when many events are combined. But still, the distribution is asymmetric and has a broader minimum than in the previous tests.

The calibration curve is shown in Figure 7.13. Slope and y-intercept have almost ideal values. Although the single data points do not lie perfectly on the fitted line, their distribution is in accordance within errors.

Again, ensemble testing yields pull distributions that resemble Gaussian distributions with a mean around 0 and a width around 1, which can be seen in Figure 7.14 for the $m_t = 175$ GeV input sample.
Pull mean and width for all samples are plotted in Figure 7.15. The results are not perfectly consistent with 0 and 1, respectively, which is not a problem in this case, since the likelihood distributions are not Gaussian.

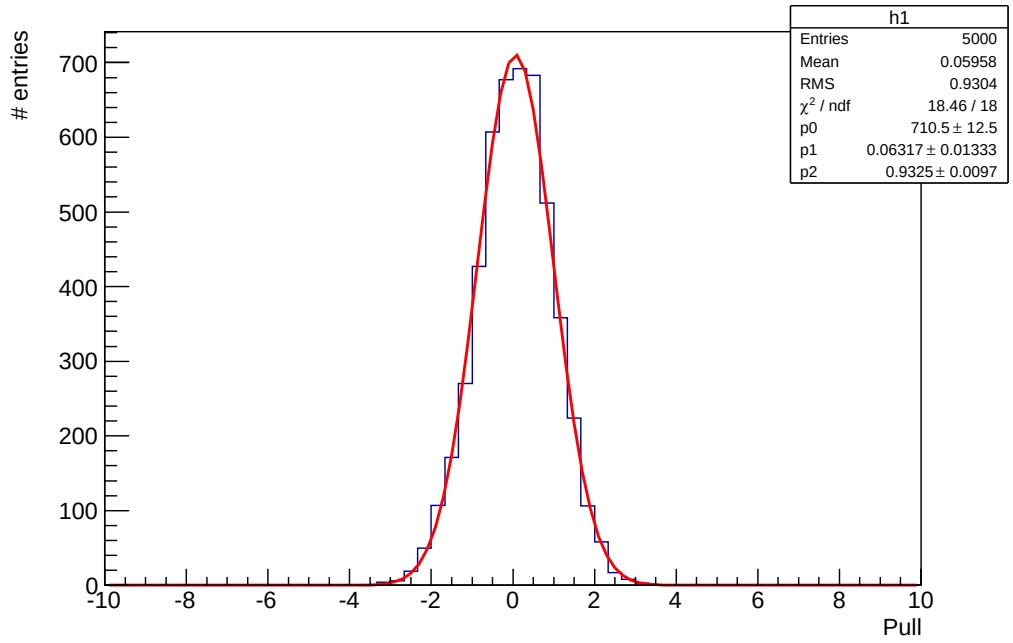

Figure 7.14.: Pull distribution with fitted Gaussian distribution for the $m_t = 175$ GeV sample with Mc10b transfer functions.

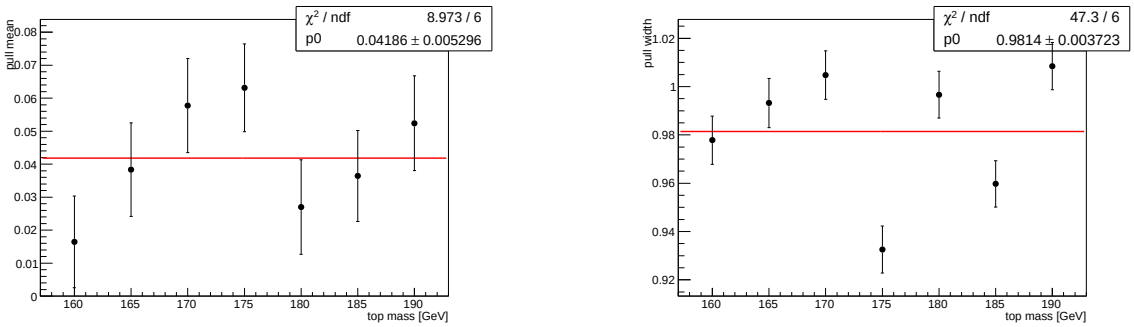

(a) pull mean

(b) pull width

Figure 7.15.: Pull mean and width for all samples with Mc10b transfer functions.

8. Tests with ATLAS Monte Carlo events

After the tests on parton-level events, NLO Monte Carlo events from the official ATLAS Monte Carlo production are used as input. The datasets used in this chapter are the $t\bar{t}$ mass variation datasets from the MC10b production round. The data has been generated by the MC@NLO matrix element calculator [44–46] with parton showering from Herwig/Jimmy [47–49]. Detector simulation has been done with Geant 4 [50, 51]. Nine signal samples are used, each corresponding to a different top quark mass: 160 GeV, 165 GeV, 167.5 GeV, 170 GeV, 172.5 GeV, 175 GeV, 177.5 GeV, 180 GeV and 190 GeV. From each sample, 1000 events are selected using the same event selection as in Chapter 7.

For the cross sections and acceptance rates, the same values as in the previous chapter are used, although the Monte Carlo events used in this chapter are NLO. The choice to still use leading order cross sections and acceptance rates is a conscious one: this way, the matrix element method stays a strict leading order method, and NLO effects are handled by calibration alone instead of changing parts of the method.

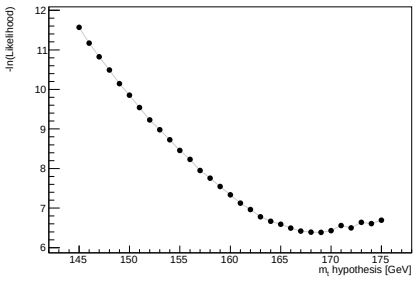

(a) single likelihood with $m_t = 160$ GeV

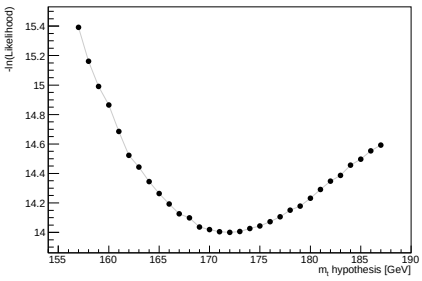

(b) single likelihood with $m_t = 172.5$ GeV

Figure 8.1.: Single event likelihood distributions for (a) an event with input top quark mass 160 GeV and (b) an event with input top quark mass 172.5 GeV, using ATLAS Monte Carlo events.

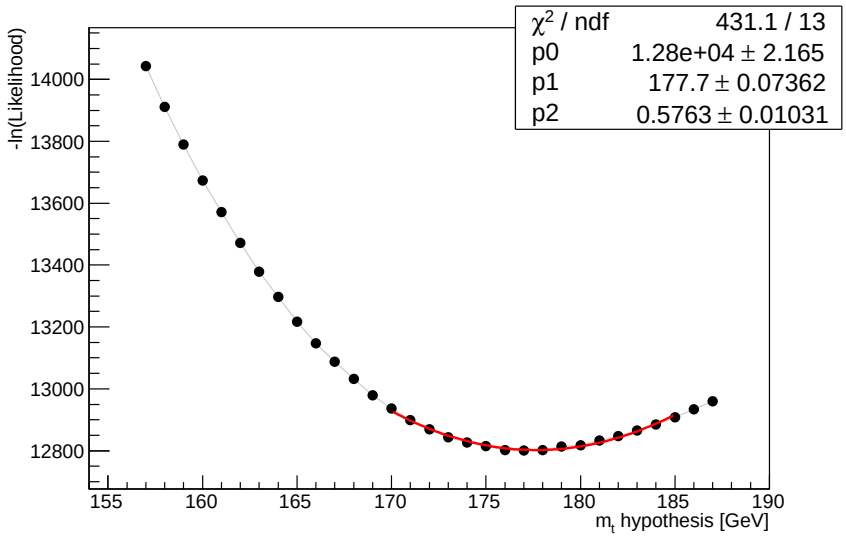

Figure 8.2.: Combined likelihood curve for 1000 events from the sample with $m_t = 172.5$ GeV using ATLAS Monte Carlo events.

Figure 8.1 shows the likelihood distributions of two single events. The combined likelihood curves for 1000 events – as shown in Figure 8.2 for an input top quark mass of $m_t = 172.5$ GeV – is asymmetric and has its minimum at 177.7 GeV, about 5 GeV higher than the input top quark mass. An asymmetric and shifted result is to be expected, though, since the Monte Carlo data contains NLO contributions and events from quark-antiquark annihilation which the matrix element method does not account for. The fraction of $t\bar{t}$ events in the samples produced by gg fusion is about 80%. $q\bar{q}$ annihilation makes up the other 20%. Another effect in the Monte Carlo samples is the change of kinematic distributions due to radiation. For the same reason, the calibration curve – shown in Figure 8.3 – is not expected to have a slope of 1 and no shift. Rather, slope and y-intercept of this calibration curve are used – as the name suggests – to calibrate the matrix element method for the use with data. After applying the matrix element method on data, one would calculate the true value for the top quark mass m_t^{true} from the measured value m_t^{meas} using the calibration curve's slope α and y-intercept β:

$$m_t^{\text{true}} = \frac{1}{\alpha}(m_t^{\text{meas}} - \beta) \quad , \tag{8.1}$$

or, in the case of a calibration curve shifted by 175 GeV,

$$m_t^{\text{true}} = \frac{1}{\alpha'}(m_t^{\text{meas}} - \beta' - 175\ \text{GeV}) + 175\ \text{GeV} \quad . \tag{8.2}$$

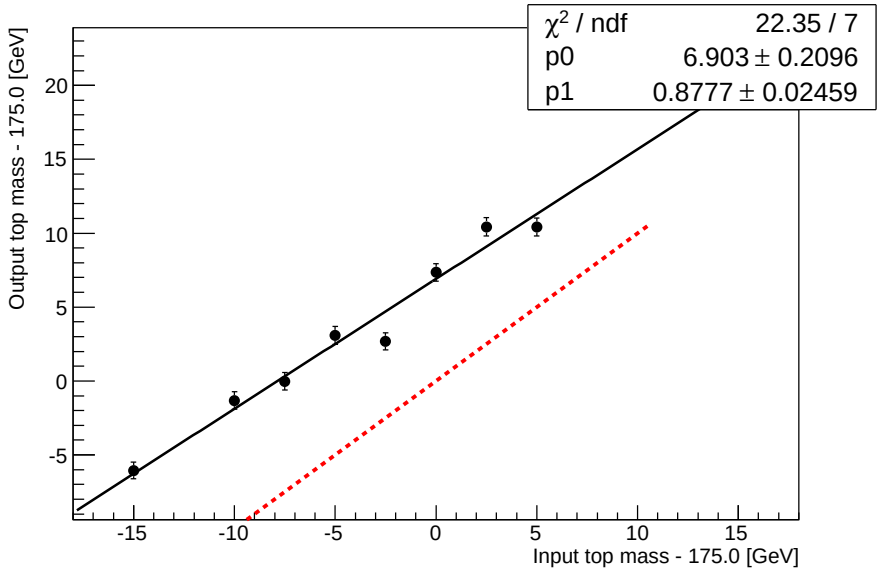

Figure 8.3.: Calibration curve for ATLAS Monte Carlo data. The dashed red line indicates a calibration curve with a slope of 1 and no offset.

The calibration curve in Figure 8.3 is shifted, and therefore Equation 8.2 should be used with values $\alpha' = 0.8777 \pm 0.02459$ and $\beta' = 6.903 \pm 0.2096$.

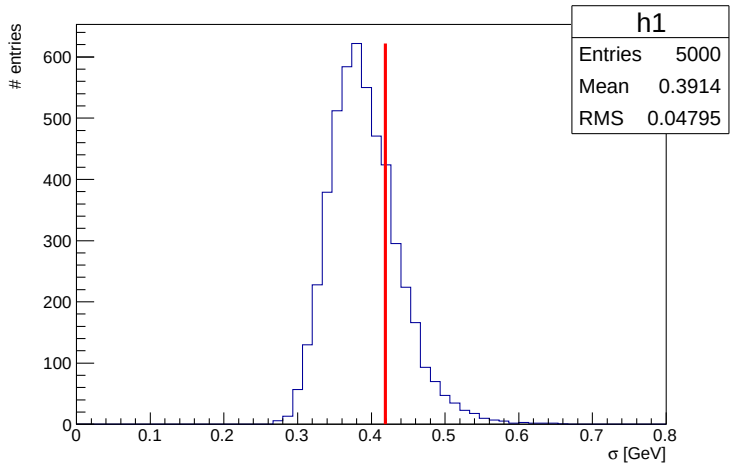

Figure 8.4.: Expected statistical uncertainty for $m_t = 172.5$ GeV for an integrated luminosity of $\int \mathcal{L} = 5.25$ fb^{-1}. The red line indicates the actual statistical uncertainty measured from 1000 events, scaled to match the integrated luminosity.

To give an overview of the expected statistical uncertainty for a measurement with the matrix element method, a distribution of the statistical uncertainty of 5000 ensembles – drawn from the $m_t = 172.5$ GeV sample – has been plotted and scaled to match the total integrated luminosity recorded by ATLAS in 2011, $\int \mathcal{L} = 5.25\ \text{fb}^{-1}$. The results are shown in Figure 8.4. The red line in the histogram indicates the statistical uncertainty measured from all 1000 events in the sample, also scaled to match the integrated luminosity. The results are in excellent agreement.

NLO contributions are not the only reason for the difference between the measured top quark masses and the input top quark masses. It is possible for events to be selected even though one or more of the particles are not part of the semileptonic $t\bar{t}$ decay, e.g. due to ISR or FSR. To study the influence of these events, samples with only matched events are selected – i.e. where each of the six final state particles is part of the $t\bar{t}$ decay. This requires information from the Monte Carlo generator to be present in the MC data sample. An event is considered matched if its Monte Carlo truth information contains a $t\bar{t}$ pair and its decay products in the semileptonic channel, and if the final state partons from this decay chain correspond to the reconstructed objects in the event. Only four samples were available which had the necessary information: the ones for the top quark masses 170 GeV, 172.5 GeV, 180 GeV and 190 GeV.

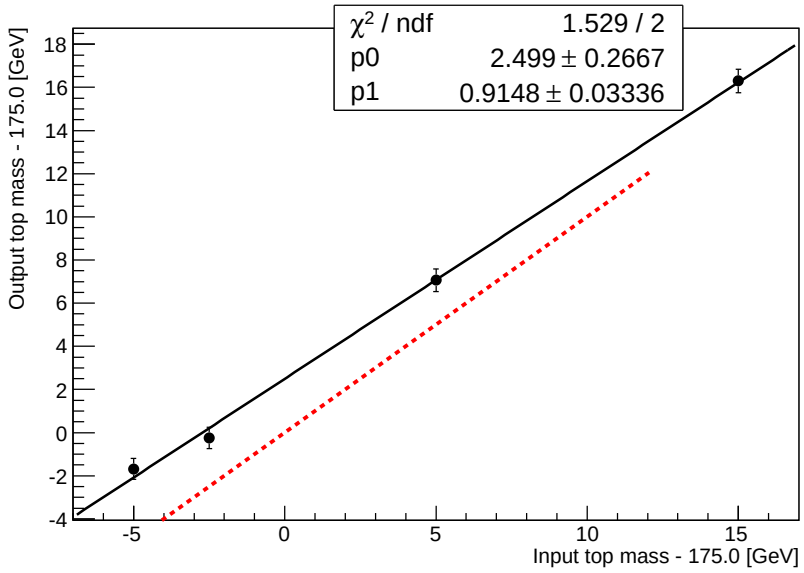

Figure 8.5.: Calibration curve for ATLAS Monte Carlo data, using only matched events.

The calibration curve for the matched samples is shown in Figure 8.5. Having a slope of 0.91 and a y-intercept of 2.5, the difference between this line and the ideal line through the origin with a slope of 1 is smaller than it was the case without matching.
For samples that contain only unmatched events, no minimum could be found in the scanned likelihood range for any of the samples. The combined likelihood curves for the $m_t = 172.5$ GeV sample containing only matched events and for the sample containing only unmatched events are shown in Figure 8.6. The contribution of the unmatched events is about 70%.

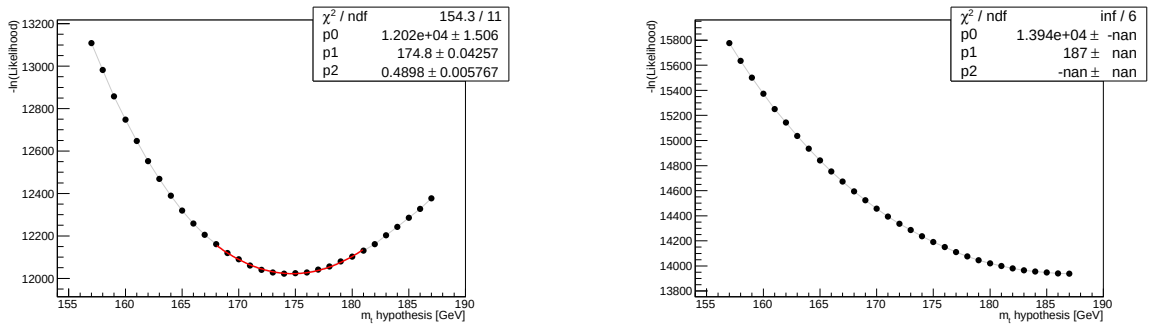

Figure 8.6.: Combined likelihood distributions for two samples with $m_t = 172.5$ GeV, containing (a) only matched events and (b) only unmatched events.

The main background contributions for the semileptonic $t\bar{t}$ channel, QCD and $W+$jets, are also studied with ATLAS Monte Carlo data. Likelihood distributions were generated for both background sources. They can be found in Figure 8.7. Especially the QCD background will need further study, as its likelihood distribution looks similar to the distribution of a $t\bar{t}$ sample.

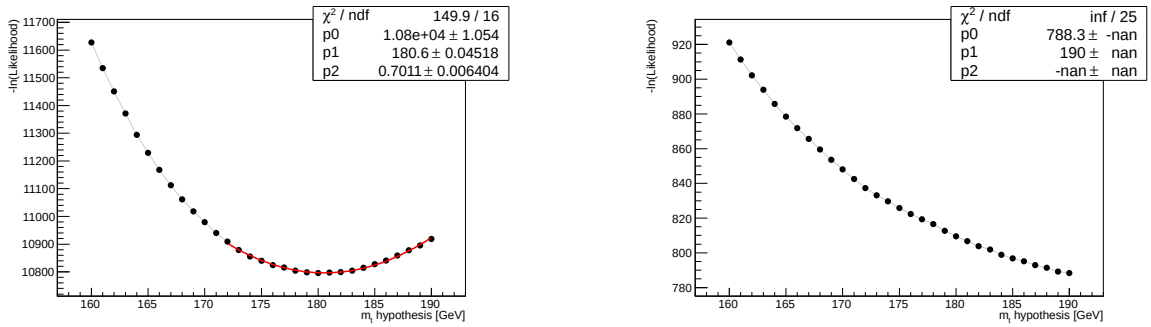

(a) QCD (b) W + jets

Figure 8.7.: Combined likelihood distributions for (a) QCD and (b) W+jets background events.

9. Systematic uncertainties

Different systematic uncertainties have to be taken into account for a measurement of the top quark mass with the matrix element method. This chapter gives an overview over the sources of some systematic uncertainties.

Likelihood minimum fit
The use of a parabola to determine minimum and width of the log-likelihood distribution is far from perfect. As shown in Chapters 7 and 8, the combined likelihood distributions are not necessarily symmetric. This could lead to a shift in the extracted minimum as well as a false estimation of the uncertainty. However, this effect is mitigated due to the fact that the parabolic fit is only performed in the region around the likelihood's minimum.

Calibration correction
Since the calibration curve for Monte Carlo data is not consistent with a slope of 1 and no offset, a linear correction would have to be applied to measured top quark masses from data. Due to limited Monte Carlo statistics, the calibration curve's values for slope and offset are subject to statistical fluctuations.

Jet energy scale
If the measurement of jet energies is not precisely calibrated, it has an effect on the measured top quark mass. The uncertainty of this jet energy scale (JES) can be studied by varying the energies of all jets and noting the difference in the measured top quark mass.
As a more advanced approach, the matrix element method can be used to fit two parameters – the top quark mass and the jet energy scale – at once. Even a three-dimensional fit with a separate jet energy scale for b-quarks is possible.

Transfer functions
The transfer functions, though fitted to Monte Carlo data, are a lot simpler than the

full detector simulation, not to mention the real detector. Therefore, there are most certainly effects that the transfer functions cannot describe perfectly, leading to a systematic uncertainty.

Approximations

Some approximations have been made over the course of this thesis, most notably the use of narrow width approximation to reduce the number of integration variables and the use of the matrix element which does not take spin correlations into account. Both approximations have an effect on the precision of the measurement.

10. Conclusion and outlook

The matrix element method has been presented as a high-precision measurement method for the top quark mass in the semileptonic channel.
A computer programme, MEMTool, has been developed to perform the likelihood calculations for the matrix element method and extract the top quark mass from the calculated likelihoods.

In tests with simulated parton-level events, which were performed to test the method, the results were correct.
The application of the method to ATLAS Monte Carlo data yielded a calibration curve that is linear, yet has a slope other than 1 and an offset greater than 0. This behaviour is expected, as the calibration curve from Monte Carlo events serves to calibrate the method for use with real data.

Before attempting a measurement on data, background contributions as well as effects from unmatched events have to be studied thoroughly, so that it is possible to generate a realistic calibration for the measurement.

The method presented in this thesis can be refined by adding matrix elements for other processes, most notably the one for $t\bar{t}$ production via quark-antiquark annihilation, but also possibly a background likelihood for W + jets.
An extension of the method to a two-dimensional fit, measuring the values of the top quark mass and the jet energy scale simultaneously, would reduce the systematic JES uncertainty. As MEMTool currently needs only 6 minutes per event on a modern computer, a simultaneous fit of top quark mass and jet energy scale is feasible, though it would of course increase the computation time.

A. Phase space transformations and reconstruction of event kinematics

This chapter contains the instructions on how to reconstruct the four-momenta of the initial partons and final state particles from the different sets of integration variables.

A.1. SimplePznuKinematic

The integration variables for `SimplePznuKinematic` are E_2, E_3, E_4, E_5, E_6 and p_7^z. η_i and ϕ_i are known for $i = 2, \dots 6$. Therefore, the momenta of the visible final state particles can easily be obtained:

$$p_{T,2} = \sqrt{E_2^2 - m_b^2} \cdot \sin\left(2\text{atan}\left(e^{-\eta_2}\right)\right)$$
$$\vec{p}_2 = p_{T,2} \cdot \begin{pmatrix} \cos\phi_2 \\ \sin\phi_2 \\ \text{sinh}\eta_2 \end{pmatrix}$$

$$p_{T,3} = \sqrt{E_3^2 - m_b^2} \cdot \sin\left(2\text{atan}\left(e^{-\eta_3}\right)\right)$$
$$\vec{p}_3 = p_{T,3} \cdot \begin{pmatrix} \cos\phi_3 \\ \sin\phi_3 \\ \text{sinh}\eta_3 \end{pmatrix}$$

$$p_{T,4} = E_4 \cdot \sin\left(2\text{atan}\left(e^{-\eta_4}\right)\right)$$
$$\vec{p}_4 = p_{T,4} \cdot \begin{pmatrix} \cos\phi_4 \\ \sin\phi_4 \\ \text{sinh}\eta_4 \end{pmatrix}$$

$$p_{T,5} = E_5 \cdot \sin\left(2\text{atan}\left(e^{-\eta_5}\right)\right)$$
$$\vec{p}_5 = p_{T,5} \cdot \begin{pmatrix} \cos\phi_5 \\ \sin\phi_5 \\ \sinh\eta_5 \end{pmatrix}$$

$$p_{T,6} = E_6 \cdot \sin\left(2\text{atan}\left(e^{-\eta_6}\right)\right)$$
$$\vec{p}_6 = p_{T,6} \cdot \begin{pmatrix} \cos\phi_6 \\ \sin\phi_6 \\ \sinh\eta_6 \end{pmatrix}$$

Conservation of energy and momentum requires

$$p_0 + p_1 - \sum_{i=2}^{7} p_i = 0 \qquad . \tag{A.1}$$

Using this and the fact that the initial partons' x- and y-momenta are assumed to be zero, one can calculate the neutrino's momentum:

$$\begin{aligned} p_7^x &= -\sum_{i=2}^{6} p_i^x \\ p_7^y &= -\sum_{i=2}^{6} p_i^y \\ E_7 &= = |\vec{p}_7| \end{aligned}$$

The other two terms from Equation A.1 are used to fix the momenta of the initial partons.

$$\begin{aligned} \zeta_1 &= \frac{1}{E_p} \sum_{i=2}^{7} E_i \\ \zeta_2 &= \frac{1}{E_p} \sum_{i=2}^{7} p_i^z \\ E_0 &= (\zeta_1 + \zeta_2) \cdot E_p \\ p_0^z &= (\zeta_1 + \zeta_2) \cdot E_p \\ E_1 &= (\zeta_1 - \zeta_2) \cdot E_p \\ p_1^z &= -(\zeta_1 - \zeta_2) \cdot E_p \end{aligned}$$

$E_p = 3500$ GeV is the energy of the incoming protons.

A.2. WmassKinematic

The calculations for this set of integration variables can be found in [52].

The integration variables for `WmassKinematic` are E_2, E_3, E_4, E_5, E_6 and $m^2_{W,lep}$. η_i and ϕ_i are known for $i = 2, \ldots 6$.

The calculations for $i = 2, \ldots 6$ and the neutrino's transverse momentum are carried out in exactly the same way as shown above in Section A.1. Then, the neutrino's z-momentum is calculated from the W boson mass.

$$m^2_{W,lep} = (p_6 + p_7)^2 = 2E_6E_7 - 2\left(p_6^x p_7^x + p_6^y p_7^y + p_6^z p_7^z\right)$$
$$\underbrace{\frac{m^2_{W,lep}}{2} + \left(p_6^x p_7^x + p_6^y p_7^y + p_6^z p_7^z\right)}_{\kappa} = E_6E_7 - p_6^z p_7^z$$

There are two possible solutions for p_7^z:

$$p_7^z = \kappa\frac{p_6^z}{p_{T6}^2} \pm \frac{1}{p_{T6}^2}\sqrt{E_6^2(\kappa - p_{T6}^2 p_{T7}^2)} \quad .$$

Afterwards, the neutrino's energy can be calculated, followed be the initial partons' momenta.

A.3. FourMassesKinematic

The integration variables for `FourMassesKinematic` are E_4, E_6, $m^2_{W,had}$, $m^2_{W,lep}$, $m^2_{t,had}$ and $m^2_{t,lep}$.
The algorithm to reconstruct all particles' four-momenta from the integration is rather sophisticated. It is an adaption of the one found in [42].

The reconstruction of $\vec{p}_4$ and $\vec{p}_6$ is trivial.

$$p_{T,4} = E_4 \cdot \sin\left(2\text{atan}\left(e^{-\eta_4}\right)\right)$$
$$\vec{p}_4 = p_{T,4} \cdot \begin{pmatrix} \cos\phi_4 \\ \sin\phi_4 \\ \sinh\eta_4 \end{pmatrix}$$

$$p_{T,6} = E_6 \cdot \sin\left(2\text{atan}\left(e^{-\eta_6}\right)\right)$$
$$\vec{p}_6 = p_{T,6} \cdot \begin{pmatrix} \cos\phi_6 \\ \sin\phi_6 \\ \sinh\eta_6 \end{pmatrix}$$

The energy of the second light jet, E_5, can be calculated using the mass of the hadronic W boson,

$$E_5 = \ = \frac{m_{W,had}^2}{2E_4(1-\cos\theta_{45})} \quad ,$$

where θ_{ij} is the angle between particle i and particle j.

$$p_{T,5} = E_5 \cdot \sin\left(2\text{atan}\left(e^{-\eta_5}\right)\right)$$
$$\vec{p}_5 = p_{T,5} \cdot \begin{pmatrix} \cos\phi_5 \\ \sin\phi_5 \\ \sinh\eta_5 \end{pmatrix}$$

Calculating the hadronic b-quark's energy is more complicated, because its mass cannot be neglected. The b-quark's absolute momentum, $\rho_2 = |\vec{p}_2|$, is:

$$\rho_2 = \frac{-M \cdot D - P \cdot \sqrt{M^2 + m_b^2(D^2+P^2)}}{D^2 - P^2} \quad \text{, with}$$
$$M = \frac{1}{2}(m_{t,had}^2 - m_{W,had}^2 - m_b^2) \quad ,$$
$$P = E_4 + E_5 \quad ,$$
$$D = E_4 \cdot \cos\theta_{24} + E_5 \cdot \cos\theta_{25} \quad .$$

Using conservation of energy and momentum (Equation A.1), the shorthand notations S_x

and S_y are defined as:

$$S_x := -p_3^x - p_7^x = p_2^x + p_4^x + p_5^x + p_6^x$$
$$S_y := -p_3^y - p_7^y = p_2^y + p_4^y + p_5^y + p_6^y$$

Another shorthand notation for the angles of a momentum is introduced, as well as a few new terms.

$$\hat{p}_i = \begin{pmatrix} \sin\theta_i \cos\phi_i \\ \sin\theta_i \sin\phi_i \\ \cos\theta_i \end{pmatrix} =: \begin{pmatrix} sc_i \\ ss_i \\ c_i \end{pmatrix}$$

S_x and S_y are combined to get rid of ρ_3 and ρ_7.

$$S_y(sc_3) - S_x(ss_3) = \rho_7(sc_7 \cdot ss_3 - ss_7 \cdot sc_3) =: \alpha_0$$
$$S_y(sc_7) - S_x(ss_7) = \rho_3(sc_3 \cdot ss_7 - ss_3 \cdot sc_7)$$

These two equations are then solved for ρ_3 and ρ_7, respectively.

$$\rho_7 = \frac{S_y(sc_3) - S_x(ss_3)}{(sc_7)(ss_3) - (ss_7)(sc_3)} \tag{A.2}$$
$$\rho_3 = \frac{S_y(sc_7) - S_x(ss_7)}{(sc_3)(ss_7) - (ss_3)(sc_7)} \tag{A.3}$$

The leptonic W boson's mass is expanded.

$$\begin{aligned} m_{W,lep}^2 &= E_{W,lep}^2 - \vec{p}_{W,lep}^{\,2} \\ &= m_6^2 + m_7^2 + 2(E_6E_7 - \vec{p}_6 \cdot \vec{p}_7) \\ \frac{m_{W,lep}^2}{2} &= E_6E_7 - \vec{p}_6 \cdot \vec{p}_7 \\ &= \rho_6\rho_7 - \rho_6\rho_7 \left(\frac{p_{x,6}p_{x,7} + p_{y,6}p_{y,7} + p_{z,6}p_{z,7}}{\rho_6\rho_7} \right) \\ \frac{m_{W,lep}^2}{2\rho_6} &= \rho_7 \left(1 - (sc_6)(sc_7) - (ss_6)(ss_7) - (c_6)(c_7)\right) \end{aligned}$$

With the definition of α_1 as

$$\alpha_1 := \frac{m_{W,lep}^2}{2\alpha_0\rho_6} \qquad ,$$

this becomes

$$\frac{\alpha_1\alpha_0}{\rho_7} = 1 - (sc_6)(sc_7) - (ss_6)(ss_7) - (c_6)(c_7) \qquad . \tag{A.4}$$

Next, Equations A.2 and A.4 are combined.

$$\frac{\alpha_1\alpha_0}{\alpha_0}[(ss_3)(sc_7) - (sc_3)(ss_7)] = 1 - (sc_6)(sc_7) - (ss_6)(ss_7) - (c_6)(c_7)$$
$$(c_6)(c_7) = 1 - [(sc_6) + \alpha_1(ss_3)](sc_7) - [(ss_6) - \alpha_1(sc_3)](ss_7)$$

$$(c_7) = \frac{1 - \beta_1(sc_7) - \beta_2(ss_7)}{(c_6)} \qquad \text{, with} \tag{A.5}$$
$$\beta_1 := (sc_6) + \alpha_1(ss_3)$$
$$\beta_2 := (ss_6) - \alpha_1(sc_3)$$

From $\sin^2 x + \cos^2 x = 1$ directly follows $(sc_7)^2 + (ss_7)^2 + (c_7)^2 = 1$.
Inserting Equation A.5 yields

$$a(sc_7)^2 + 2b(sc_7)(ss_7) + c(ss_7)^2 + 2d(sc_7) + 2e(ss_7) + f = 0 \tag{A.6}$$

with

$$\begin{aligned} a &= (c_6)^2 + \beta_1^2 \\ b &= \beta_1\beta_2 \\ c &= (c_6)^2 + \beta_2^2 \\ d &= -\beta_1 \\ e &= -\beta_2 \\ f &= 1 - (c_6)^2 \qquad . \end{aligned}$$

Next, $m_{t,lep}$ is used.

$$\begin{aligned} m_{t,lep}^2 &= E_{t,lep}^2 - \vec{p}_{t,lep}^{\,2} \\ &= m_{W,lep}^2 + m_b^2 + 2(E_{W,lep}E_3 - \vec{p}_{W,lep} \cdot \vec{p}_3) \end{aligned}$$

A new variable M_l is defined.

$$\begin{aligned} M_l &:= \frac{1}{2}(m_{t,lep}^2 - m_{W,lep}^2 - m_b^2) \\ \Rightarrow \quad M_l &= E_{W,lep}E_3 - \vec{p}_{W,lep} \cdot \vec{p}_3 \\ &= (E_6 + E_7)E_3 - (\vec{p}_6 + \vec{p}_7) \cdot \vec{p}_3 \\ &= \rho_6 E_3 + \rho_6 E_3 - \rho_6\rho_7 \cos\theta_{336} - \rho_6\rho_7 \left(\frac{\vec{p}_3 \cdot \vec{p}_7}{\rho_3\rho_7}\right) \end{aligned}$$

From this point on, E_3 will be written as $E_3 := \rho_3(1+\delta)$. δ is a nuisance parameter; it is first approximated as zero and then, after having calculated ρ_3, δ is adjusted accordingly and another iteration of the calculations from here on is done.

$$M_l = \rho_3\rho_6(1 + \delta - \cos\theta_{36}) + \rho_3\rho_7 \left(1 + \delta - \frac{\vec{p}_3 \cdot \vec{p}_7}{\rho_3\rho_7}\right) \tag{A.7}$$

$$\frac{M_l}{\rho_3} = d_0 + \rho_7[1 - (sc_7)(sc_3) - (ss_7)(ss_3) - (c_7)(c_3)] \tag{A.8}$$

with $d_0 := \rho_6(1 + \delta - \cos\theta_{36})$.
Equations A.2 and A.5 are inserted into this:

$$\begin{aligned} \frac{M_l}{\rho_3} &= d_0 + \frac{\alpha_0}{(sc_7)(ss_3) - (ss_7)(sc_3)} \\ &\quad \times \left[1 + \delta - (sc_7)(sc_3) - (ss_7)(ss_3) - \frac{1 - \beta_1(sc_7) - \beta_2(ss_7)}{(c_6)}(c_3)\right] \end{aligned}$$

$$\frac{M_l}{\rho_3} = \frac{\gamma_0 + \gamma_1(sc_7) + \gamma_2(ss_7)}{(sc_7)(ss_3) - (ss_7)(sc_3)} \tag{A.9}$$

with

$$\begin{aligned} \gamma_0 &= \alpha_0 \left(1 + \delta - \frac{(c_3)}{(c_6)}\right) \\ \gamma_1 &= d_0(ss_3) - \alpha_0(sc_3) + \frac{\alpha_0\beta_1(c_3)}{(c_6)} \\ \gamma_2 &= -d_0(sc_3) - \alpha_0(ss_3) + \frac{\alpha_0\beta_2(c_3)}{(c_6)} \end{aligned}$$

Equation A.3 is inserted into Equation A.9:

$$\frac{-M_l(sc_3)(ss_7) + M_l(ss_3)(sc_7)}{S_x(ss_7) - S_y(sc_7)} = \frac{\gamma_0 + \gamma_1(sc_7) + \gamma_2(ss_7)}{(sc_7)(ss_3) - (ss_7)(sc_3)}$$

$$A(sc_7)^2 + 2B(sc_7)(ss_7) + C_(ss_7)^2 + 2D_2(sc_7) + 2E(ss_7) = 0 \tag{A.10}$$

with

$$\begin{aligned} A &= M_l(ss_3)^2 + \gamma_1 S_y \\ B &= -M_l(ss_3)(sc_3) - \frac{1}{2}\gamma_1 S_x + \frac{1}{2}\gamma_2 S_y \\ C &= M_l(sc_3)^2 - \gamma_2 S_x \\ D_2 &= \frac{1}{2}\gamma_0 S_y \\ E &= -\frac{1}{2}\gamma_0 S_x \end{aligned}$$

Equation A.10 is multiplied with $(cdiv) := \frac{c}{C}$ and subtracted from Equation A.6:

$$a'(sc_7)^2 + 2b'(sc_7)(ss_7) + 2d'(sc_7) + 2e'(ss_7) + f = 0$$

with

$$\begin{aligned} a' &= a - (cdiv)A \\ b' &= b - (cdiv)B \\ d' &= d - (cdiv)D_2 \\ e' &= e - (cdiv)E \end{aligned}$$

Solving this for (ss_7) yields

$$(ss_7) = \frac{-f - a'(sc_7)^2 - 2d'(sc_7)}{2b'(sc_7) + 2e'} \quad . \tag{A.11}$$

Inserting Equation A.11 into Equation A.6 to replace all (ss_7) terms and grouping by (sc_7) gives the following fourth order polynomial:

$$\beta_4(sc_7)^4 + \beta_3(sc_7)^3 + \beta_2(sc_7)^2 + \beta_1(sc_7) + \beta_0 = 0 \tag{A.12}$$

with

$$
\begin{aligned}
\beta_4 &= a'^2c + 4ab'^2 + 4b\Lambda_3 \\
\beta_3 &= 8ab'e' + 8db'^2 + cG_3 + 4b\Lambda_2 + 4e\Lambda_3 \\
\beta_2 &= 4ae'^2 + 16db'e' + 4b'^2f + cG_2 + 4b\Lambda_1 + 4e\Lambda_1 \\
\beta_1 &= 8de'^2 + 8b'e'f + 4e\Lambda_1 + 4b\Lambda_0 + cG_1 \\
\beta_0 &= cf^2 + 4e\Lambda_0 + 4fe'^2 \\
G_3 &= 4d'a' \\
G_2 &= 2a'f + 4d'^2 \\
G_1 &= 4d'f \\
\Lambda_3 &= -a'b' \\
\Lambda_2 &= -a'e' - 2b'd' \\
\Lambda_1 &= -2d'e' - fb' \\
\Lambda_0 &= -fe'
\end{aligned}
$$

Equation A.12 has 4 solutions, up to two of which are real. With these, one solves Equation A.11, then EquationA.5, followed by Equations A.2 and A.3.
Both solutions are checked for consistency (e.g. $(sc_7)^2 + (ss_7)^2 + (c_7)^2$ has to be ≈ 1).
From the solution for ρ_3, a better approximation for the nuisance parameter δ can be obtained:

$$\delta = 1 - \frac{\sqrt{\rho_3^2 - m_b^2}}{\rho_3} \quad . \tag{A.13}$$

If two valid solutions for ρ_3 exist, the larger one is used.

With the new value for δ, all calculations starting from Equation A.7 are repeated once more.

Finally, the initial partons' momenta are calculated in the same way as in Section A.1.

Bibliography

[1] The D0 Collaboration, "A Precision Measurement of the Mass of the Top Quark", *Nature* **429:638-642,2004** (2004) arXiv:hep-ex/0406031.

[2] The D0 Collaboration, "Precise measurement of the top-quark mass from lepton+jets events at D0", *Phys.Rev.D* **84:032004,2011** (2011) arXiv:1105.6287.

[3] D. Griffiths, "Introduction to Elementary Particles", John Wiley & Sons, New York, USA, 1987.

[4] P. W. Higgs, "Broken symmetries, massless particles and gauge fields", *Phys. Lett.* **12** (1964) 132–133.

[5] Tevatron Electroweak Working Group, "Combination of cdf and do results on the mass of the top quark using up to 5.8 fb-1 of data", arXiv:1107.5255.

[6] The CDF Collaboration, "Observation of top quark production in $\bar{p}p$ collisions", *Phys. Rev. Lett.* **74** (1995) 2626–2631, arXiv:hep-ex/9503002.

[7] The D0 Collaboration, "Observation of the top quark", *Phys. Rev. Lett.* **74** (1995) 2632–2637, arXiv:hep-ex/9503003.

[8] J. Pumplin *et al.*, "New generation of parton distributions with uncertainties from global QCD analysis", *JHEP* **07** (2002) 012, arXiv:hep-ph/0201195.

[9] A. D. Martin, W. J. Stirling, R. S. Thorne, and G. Watt, "Parton distributions for the LHC", *Eur.Phys.J.C* **63:189-285,2009** (2009) arXiv:0901.0002.

[10] N. Kidonakis, "Top quark pair and single top production at Tevatron and LHC energies", arXiv:1008.2460.

[11] N. Kidonakis, "Higher-order corrections to top-antitop pair and single top quark production", arXiv:0909.0037.

[12] The D0 Collaboration, "Observation of Single Top-Quark Production", *Phys.Rev.Lett.* **103:092001,2009** (2009) arXiv:0903.0850.

[13] P. de Jong, "Top Physics at the LHC", arXiv:0902.4798.

[14] N. Kidonakis, "Heavy-Flavor Production at Accelerators", *Nucl.Phys.A* **827:448c-453c,2009** (2009) arXiv:0901.2155.

[15] N. Kidonakis, "Single top quark production cross section at hadron colliders", *PoS DIS* **2010:196,2010** (2010) arXiv:1005.3330.

[16] J. M. Campbell, R. Frederix, F. Maltoni, and F. Tramontano, "NLO predictions for t-channel production of single top and fourth generation quarks at hadron colliders", *JHEP* **10(2009)042** (2009) 10042, arXiv:0907.3933.

[17] J. Wang, C. S. Li, H. X. Zhu, and J. J. Zhang, "Factorization and resummation of t-channel single top quark production", arXiv:1010.4509.

[18] The CDF Collaboration, "First Observation of Electroweak Single Top Quark Production", *Phys.Rev.Lett.* **103:092002,2009** (2009) arXiv:0903.0885.

[19] K. Nakamura et al. (Particle Data Group), "Review of Particle Physics", *J. Phys. G* **37, 075021** (2010).

[20] M. Goebel, for the Gfitter group, "Status of the global fit to electroweak precisions data", arXiv:1012.1331.

[21] M. W. Grunewald, "Precision Electroweak Measurements and Constraints on the Standard Model", arXiv:1012.2367.

[22] The D0 Collaboration, "Measurement of ttbar production in the tau + jets topology using ppbar collisions at $\sqrt{s} = 1.96$ TeV", *Phys. Rev.* **D82** (2010) 071102, arXiv:1008.4284.

[23] The ATLAS Collaboration, "Measurement of the top quark-pair production cross section with ATLAS in *pp* collisions at $\sqrt{s} = 7$ TeV", *The European Physical Journal C - Particles and Fields* **71** (2011) 1–36, 10.1140/epjc/s10052-011-1577-6.

[24] The CMS Collaboration, "Measurement of the $t\bar{t}$ production cross section in *pp* collisions at 7 TeV in lepton + jets events using *b*-quark jet identification", *Phys. Rev. D* **84** (2011) 092004.

[25] The CMS Collaboration, "Measurement of the $t\bar{t}$ production cross section in pp collisions at $\sqrt{s} = 7$ TeV using the kinematic properties of events with leptons and jets", *The European Physical Journal C - Particles and Fields* **71** (2011) 1–27, 10.1140/epjc/s10052-011-1721-3.

[26] The CMS Collaboration, "Measurement of the $t\bar{t}$ production cross section and the top quark mass in the dilepton channel in pp collisions at $\sqrt{s} = 7$ TeV", *Journal of High Energy Physics* **2011** (2011) 1–49, 10.1007/JHEP07(2011)049.

[27] The CMS Collaboration, "First measurement of the cross section for top-quark pair production in proton–proton collisions at $\sqrt{s} = 7$ TeV", *Physics Letters B* **695** (2011), no. 5, 424 – 443.

[28] G. Aad *et al.*, "Measurement of the top quark pair production cross-section with ATLAS in the single lepton channel", `arXiv:1201.1889`.

[29] G. Aad *et al.*, "Measurement of the top quark pair production cross section in pp collisions at in dilepton final states with ATLAS", *Physics Letters B* **707** (2012), no. 5, 459 – 477.

[30] R. Schwienhorst, "Single top quark production and Vtb at the Tevatron", `arXiv:1009.5629`.

[31] The CDF and D0 Collaborations, "Combination of cdf and d0 measurements of the w boson helicity in top quark decays", Tech. Rep. CDF Note 10622-CONF, D0 Note 6231-CONF, 2011.

[32] The CDF Collaboration, "Exclusion of an Exotic Top Quark with -4/3 Electric Charge Using Soft Lepton Tagging", *Phys. Rev. Lett.* **105** (2010) 101801, `arXiv:1006.4597`.

[33] The ATLAS Collaboration, "The ATLAS Experiment at the CERN Large Hadron Collider", *JINST* **3** (2008) S08003.

[34] The CDF Collaboration, "Measurement of the Top Quark Mass with the Dynamical Likelihood Method using Lepton plus Jets Events with b-tags in ppbar Collisions at s**(1/2) = 1.96 TeV", *Phys.Rev.D* **73:092002,2006** (2006) `arXiv:hep-ex/0512009`.

[35] The ATLAS Collaboration, "Measurement of the top-quark mass using the template method in pp collisions at root(s)=7 tev with the atlas detector", Tech. Rep. ATLAS-CONF-2011-033, CERN, Geneva, 2011.

[36] `svn+ssh://svn.cern.ch/reps/atlasgrp/Institutes/Goettingen/Carsten/MEMTool`.

[37] G. P. Lepage, "A New Algorithm for Adaptive Multidimensional Integration", *J. Comput. Phys.* **27** (1978) 192.

[38] G. Lepage, "VEGAS – An Adaptive Multi-dimensional Integration Program", *Cornell Preprint* **CLNS-80/447** (1980).

[39] M. Galassi et al., "GNU Scientific Library Reference Manual (3rd Ed.)", Network Theory Ltd, 2009.

[40] J. Alwall *et al.*, "MadGraph 5 : Going Beyond", *JHEP* **1106** (2011) 128, arXiv:1106.0522.

[41] R. Kleiss and W. Stirling, "Top quark production at hadron colliders: some useful formulae", *Z.Phys.* **C40** (1988) 419–423.

[42] B. N. Mohr, "A precise measurement of the top quark mass", PhD thesis, University of California, 2007. Ph.D. thesis (advisor: Jay Hauser),

[43] V.M. Abazov et al., "Measurement of the top quark mass in the lepton + jets final state with the matrix element method", *Phys. Rev. D* **74** (2006) 092005.

[44] S. Frixione and B. R. Webber, "Matching NLO QCD computations and parton shower simulations", *JHEP* **0206** (2002) 029, arXiv:hep-ph/0204244.

[45] S. Frixione, P. Nason, and B. R. Webber, "Matching NLO QCD and parton showers in heavy flavor production", *JHEP* **0308** (2003) 007, arXiv:hep-ph/0305252.

[46] S. Frixione, F. Stoeckli, P. Torrielli, and B. R. Webber, "NLO QCD corrections in Herwig++ with MC@NLO", *JHEP* **1101** (2011) 053, arXiv:1010.0568.

[47] G. Corcella *et al.*, "HERWIG 6: An Event generator for hadron emission reactions with interfering gluons (including supersymmetric processes)", *JHEP* **0101** (2001) 010, arXiv:hep-ph/0011363.

[48] G. Corcella *et al.*, "HERWIG 6.5 release note", arXiv:hep-ph/0210213.

[49] J. M. Butterworth, J. R. Forshaw, and M. H. Seymour, "Multiparton interactions in photoproduction at HERA", *Z. Phys.* **C72** (1996) 637–646, arXiv:hep-ph/9601371.

[50] S. Agostinelli *et al.*, "GEANT4: A Simulation toolkit", *Nucl.Instrum.Meth.* **A506** (2003) 250–303.

[51] J. Allison et al., "Geant4 developments and applications", *IEEE Transactions on Nuclear Science* **53** (2006) 270–278.

[52] A. Knue, "Studies with the Matrix Element Method using the example of a top quark mass measurement with the ATLAS experiment", Master's thesis, Georg-August-Universität Göttingen, 2009.

Erklärung nach §18(8) der Prüfungsordnung für den Bachelor-Studiengang Physik und den Master-Studiengang Physik an der Universität Göttingen:

Hiermit erkläre ich, dass ich diese Abschlussarbeit selbstständig verfasst habe, keine anderen als die angegebenen Quellen und Hilfsmittel benutzt habe und alle Stellen, die wörtlich oder sinngemäß aus veröffentlichten Schriften entnommen wurden, als solche kenntlich gemacht habe.
Darüber hinaus erkläre ich, dass diese Abschlussarbeit nicht, auch nicht auszugsweise, im Rahmen einer nichtbestandenen Prüfung an dieser oder einer anderen Hochschule eingereicht wurde.

Göttingen, den 22. Februar 2012

(Carsten Brachem)